Development of an ytterbium Rydberg experiment with a nanofibre as a waveguide for Rydberg excitation light

Knut Domke
Matr. Nr.: 50089974

Masterarbeit in Physik
angefertigt im Institut für Angewandte Physik

vorgelegt der
Mathematisch-Naturwissenschaftlichen Fakultät
der
Rheinischen Friedrich-Wilhelms-Universität
Bonn

June 2025

I hereby declare that the work presented here was formulated by myself and that no sources or tools other than those cited wered used

Bonn, 04.06.2025 .....,
Date Signature

1. Supervisor: Prof. Dr. Sebastian Hofferberth

2. Supervisor: Prof. Dr. Daqing Wang

Contents

CHAPTER 1

Introduction

In the past decades, significant advancements have been accomplished in the realm of quantum non-linear optics [1], wherein individual photons are induced to engage in strong mutual interactions [2]. These interactions are of great fundamental and technological interest, as they form the foundation of optical quantum information processing [3]. The generation of effective photon-photon interactions through strong coupling to matter therefore evolved to an important research topic in recent years [2]. The interaction of a single photon with an atom is in general quite weak due to the small absorption cross-section of an atom on resonance [2]. To enhance this and achieve a well-controllable light-matter interaction, many different platforms have been developed over the years. Resonant structures, as in cavity quantum electrodynamics (QED) experiments, for example, where atoms are trapped in a high-finesse optical resonator, increase the coupling probability by allowing many interactions with the same photons [4]. Another approach addresses this problem through Rydberg quantum optics [5, 6]. Due to their strong van der Waals interactions, Rydberg atoms can be used to create strong nonlinearities in an optical medium [7]. An effect that is a key concept for quantum information and simulation is the Rydberg blockade [7, 8]. An atom that is driven by a laser towards a Rydberg state can effectively prevent the excitation of another atom by the same laser within a certain distance. This is called the Rydberg blockade effect. The concept of a Rydberg superatom [7, 9], which is a cloud of atoms that is fully blockaded, thus acting as a single two-level system that then strongly interacts with a single photon due to the collective enhancement, is of particular interest. Waveguide QED, in which single quantum emitters are coupled to photons propagating in a waveguide, is another powerful platform for enhanced interaction [10], featuring strong optical mode confinement to the waveguide. This results in a much stronger atom-photon interaction than in free space [10].
Although all of these platforms demonstrate remarkable capabilities on their own in the single-emitter-photon coupling strength, they still face a lot of challenges in scaling to the many-body regime of quantum non-linear optics [2]. This thesis introduces an experimental platform that synergizes Rydberg superatoms [7, 9] and waveguide QED by the super-extended evanescent field of optical nanofibers [11], with the aim of overcoming the aforementioned challenges and reaching the many-body regime of quantum non-linear optics.
In this thesis I start by introducing the theoretical basics of optical fibers and tapered optical fibers in chapter 2. In chapter 3 I briefly present the idea of the overall experimental platform and the evanescent field of optical nanofibers that make this possible. This also motivates the work I did in

my thesis. The nanofibers for the project need to be tested in a dust-free environment and also under vacuum conditions. Therefore, I built a fiber testing table with a vacuum chamber, a clean air working hood, and an optical setup for the transmission analysis of the nanofibers which I present in chapter 4. The following chapter 5 presents the fiber preparation steps, the general testing of the transmission of nanofibers that I carried out under different conditions, and the observations I made. This chapter continues with a collection of observations that I made while testing just the fiber material for its response on the intended laser wavelength for the project and ends with a discussion of those. In chapter 6 I propose three new ideas for solutions of the problems that occurred while testing the fibers in 5 and discuss their feasibility and current development status. Finally, in chapter 7 I conclude this thesis with a summary of the achievements of this thesis and my participation in this project, as well as an outlook on how these findings can be used on future research steps.

CHAPTER 2

Fibers and nanofibers

In this chapter, important concepts are established to build the foundational knowledge needed to understand the properties and characteristics of tapered and non-tapered optical fibers. The basics of step-index optical fibers and tapered optical fibers as well as their mode structure are covered here.

2.1 Step-index optical fibers

Due to their high isolation from environmental interference, light weight, low production cost, and high-bandwidth low-loss information transport [12], optical fibers are used in telecommunications as a standard solution for low-loss light signal transmission and form the backbone of our technological infrastructure. For this application, step-index optical fibers are often used [12]. They are long, very thin dielectric cylindrical waveguides made from two layered high purity fused silica (SiO_2). The inner layer is denoted as the core with a refractive index n_{co} that is surrounded by a second layer, the cladding, with a refractive index n_{cl}, see figure 2.1. The refractive index of the air or vacuum around the fiber is denoted by n_0.

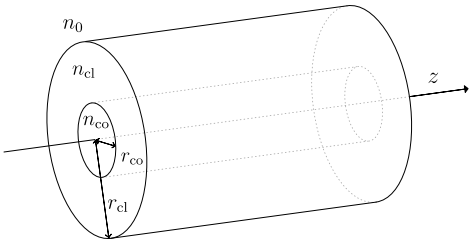

Figure 2.1: Step-index fiber with a core with refractive index n_{co} and radius r_{co}, as well as the cladding with refractive index n_{cl} and radius r_{cl}

Most of the power of light in such a fiber is guided by the core by total internal reflection (TIR) on the core-cladding interface[13]. For this phenomenon to occur, the incident angle θ of the light must be larger than the critical angle θ_c and the refractive index of the core must be higher than that of the cladding $n_{\mathrm{co}} > n_{\mathrm{cl}}$. Otherwise, light leaks out of the core into the cladding and is lost. The critical angle θ_c can be calculated by applying Snell's law [13]

$$\theta_c = \arcsin\left(n_{\mathrm{cl}}/n_{\mathrm{co}}\right) \quad \text{for} \quad n_{\mathrm{cl}} \leq n_{\mathrm{co}}. \tag{2.1}$$

Figure 2.2 shows the step-wise jump in refractive index between the core and the cladding that gives the step index fibers their name.

In practice, this stepwise jump in refractive index is achieved by doping the core with rare earth

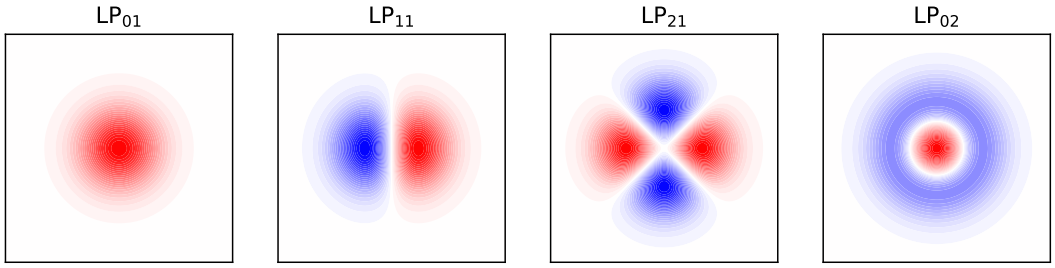

Figure 2.3: Electric field amplitude profile of the four lowest LP_{lm} modes

materials such as erbium (Er), ytterbium (Yb), thulium (Tm), or germanium (Ge), which is a metalloid. In contrast, the cladding is often pure silica for such fibers. Other concepts in which the cladding is doped with fluorine (F) and the core is made of pure silica have advantages over the former in radiation resistance and an improved UV light and mid-IR transmission [14]. Typically, for step-index fibers, the difference in the refractive indices of the core and the cladding is only 1%. This small difference in refractive index with regard to Eq. (2.1) leads to the condition that only incident rays near parallel to the fiber axis will be guided. That is why they are also called weakly guiding [15]. The propagating field modes can be calculated by solving the Maxwell equations. As has been done many times in the literature before [15–17], this section will therefore qualitatively cover the most relevant properties of fiber core guided modes based on the mentioned textbooks and the work of Lundgaard Sørensen [18] and Sagué Cassany [19].

As exact solutions are lengthy and cumbersome, Gloge [20] constructed a set of approximate solutions of the Maxwell equations using the assumption of a weakly guiding fiber, as the field can be regarded transverse to the fiber axis (paraxial), allowing the longitudinal components to be disregarded. The solutions exhibit near-linear polarization, which is why these modes are referred to as approximately linearly polarized (LP_{lm}) modes. For every azimuthal index $l = 0, 1, \ldots$, there is a series of radial solutions $m = 1, 2, \ldots$, each representing a guided mode within the fiber. Figure 2.3 illustrates the intensity distribution for the four lowest-order core-guided LP_{lm} modes. The LP_{01} mode is the lowest order mode, also called the fundamental mode. This mode is predominantly excited when the incoming light is a Gaussian beam, as it resembles a Gaussian distribution [15].

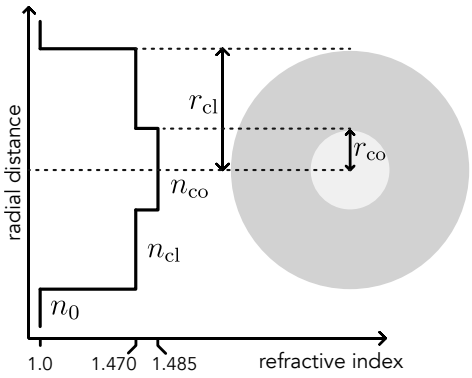

Figure 2.2: Step-index fiber with higher uniform refractive index in the core than in the cladding with a step-like change on the core-cladding interface

In conventional step-index optical fibers, the proportion of the core radius r_{co} to that of the cladding r_{cl} typically falls between 1/100 and 1/10. Because of the small refractive index difference between the cladding and the core, the field distribution of the modes in the fiber extends into the cladding as an evanescent field. This is also why a large cladding radius is necessary in the first place. A part of the mode therefore propagates outside the core, which is one of the theoretical foundations for the following chapters.

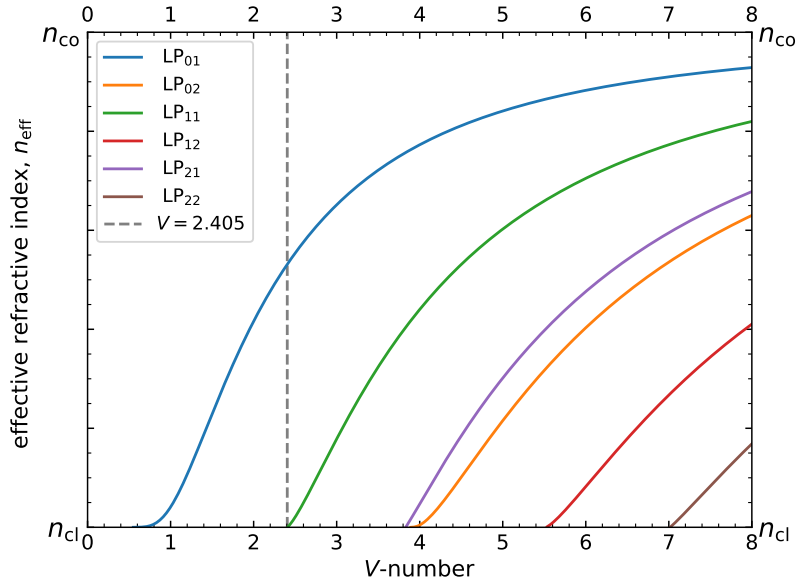

Figure 2.4: Effective refractive index as a function of the V-number for the six lowest order LP_{lm} modes, the vertical line at $V = 2.405$ indicates the cutoff below which only LP_{01} can propagate

For each mode, there exists a specific propagation constant

$$\beta_{lm} = 2\pi \frac{n_{\mathrm{eff},lm}}{\lambda} \tag{2.2}$$

such that the solution of the electric field $\mathbf{E}_{lm}$ inside the fiber with z as the propagation direction is of the form [19]

$$\mathbf{E}_{lm} \propto \exp\left[-i(\beta_{lm} z - \omega t)\right], \tag{2.3}$$

with $\omega = 2\pi f$ where f is the optical frequency and $n_{\mathrm{eff},lm}$ is the effective mode refractive index with $\lambda = 2\pi/k_0$ being the wavelength in free space. The electric field distribution for each specific mode LP_{lm} remains unchanged as it propagates in the fiber, but the phase accumulates at a constant rate β_{lm} per meter. The effective refractive index n_{eff} of a mode tells us how tightly it is confined to the fiber core, $n_{\mathrm{cl}} < n_{\mathrm{eff}} < n_{\mathrm{co}}$ being the condition for a mode to be guided by the core. Modes that do not fulfill this condition are unguided or radiating modes. For $n_{\mathrm{cl}} \sim n_{\mathrm{eff}}$ the mode is weakly confined and for $n_{\mathrm{co}} \sim n_{\mathrm{eff}}$ tightly confined to the core. In figure 2.4 the relative effective refractive index n_{eff} for the lowest-order LP modes is plotted as a function of the dimensionless V-number. It is also known as the normalized frequency and given by

$$V = 2\pi \frac{r_{\mathrm{co}}}{\lambda} \sqrt{n_{\mathrm{co}}^2 - n_{\mathrm{cl}}^2} = 2\pi \frac{r_{\mathrm{co}}}{\lambda}\ \mathrm{NA}. \tag{2.4}$$

Given a specific wavelength, core diameter and NA, the V-number determines the number of core guided modes the fiber can support.

As used in equation (2.4), the refractive indices of the cladding n_{cl} and the core n_{co} also define a

fundamental property of an optical fiber called the numerical aperture (NA) with

$$\mathrm{NA} = \sqrt{n_{\mathrm{co}}^2 - n_{\mathrm{co}}^2}. \tag{2.5}$$

It is comparable to the numerical aperture of a lens and is often one of the specifications of a fiber given by the manufacturer.

As can be seen in figure 2.4 which represents the general case for all fibers in the weakly guiding regime, for $V \leq 2.405$, there is only one core-guided solution, the LP_{01} mode. Such a fiber is called single-mode. This mode has no cut-off value, since its effective refractive index n_{eff} approaches zero only asymptotically when the fiber parameters are chosen such that V approaches zero. For $V > 2.405$, there is more than one core-guided mode solution. Such a fiber is called multimode. Even though a single-mode fiber only supports a single guided core mode, it can still have many allowed cladding and radiation modes.

2.2 Tapered optical nanofibers

Now that the basic concepts of step index fibers are established, the concept of tapering optical fibers to sub-wavelength diameters is introduced. Such fibers are also termed nanofibers. The process of fabricating nanofibers is discussed in detail by Warken [21] and Lundgaard Sørensen [18]. The theory of guided modes in nanofibers is discussed in detail by Sagué Cassany [19] and Kien et al. [22]. This section gives a brief overview on this topic on the basis of their work.

As described above, most of the power of the light is guided by the core as a result of total internal reflection at the cladding interface. As part of the total internal reflection, an evanescent field evolves in the cladding, which decays exponentially in the radial direction. The penetration depth of this field into the cladding depends on the propagating wavelength, the radius of the core, and the core and cladding material involved, respectively, their refractive indices, and the difference between them. To protect the light mode from environmental influences, the cladding usually has a diameter of 125 μm which is sufficient, as the penetration depth of the evanescent field is of the magnitude of the propagating wavelength. However, access to the evanescent field from the outside is of great interest for light-matter interaction. To gain access to the evanescent field, a multitude of possibilities evolved over the years, reaching from mechanical reduction of the cladding diameter by milling to chemical etching away the outer layers of the cladding.

Another solution is the tapering of standard step-index single-mode optical fibers by locally heating the fiber and pulling it apart. The evolving shape of such a tapered fiber has been modeled by Birks et al. [23]. Their model is constrained to two crucial assumptions; the fiber is heated uniformly and the section that is heated is always cylindrical. The theories developed later by Eggers et al. [24] and Baker et al. [25] that include fluid dynamics in modeling allow the use of less uniform heating sources such that a hydrogen flame can be used for the tapering process.

Figure 2.5 shows an illustration of a tapered optical fiber with a near constant waist diameter and exponential tapers. By tapering the fiber, the ratio of the cladding d_{cl} to the diameter of the core d_{co} stays constant while the overall structure gets thinner. Therefore, the effective refractive index of the core-guided modes as seen in figure 2.4 decreases with V, respectively, with the core radius in the

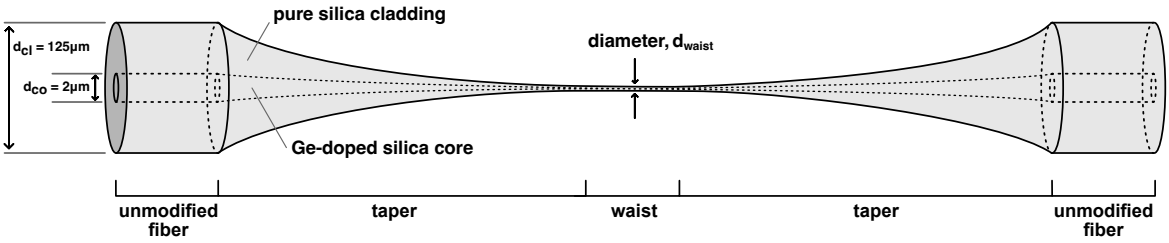

Figure 2.5: Tapered optical nanofiber with the transition (taper) and waist region being indicated. The waist is of uniform diameter. It shows the basic structural change in the fiber by tapering and the typical dimensions d_{co} and d_{cl} of a fiber.

tapers as this is the parameter thats being varied for V. By further decreasing the diameter of the fiber, the condition $n_{\mathrm{eff}} \approx n_{\mathrm{cl}}$ is eventually met for the fundamental mode. A shift occurs in which the fundamental mode transitions from core-guided to cladding-guided [26]. The air surrounding the cladding now acts as the medium with lower refractive index, so it can be considered to be the new cladding of the nanofiber, such that guided modes still exist.

One of the biggest challenges in the fabrication of nanofibers is achieving a fundamental mode transition in the tapers that is as lossless as possible. To accomplish this, the tapers should ideally change gradually throughout their whole length. For a taper to be considered approximately adiabatic according to Love et al. [26], it must have sufficiently small taper angles throughout, minimizing any power loss from the fundamental mode as it propagates along the taper. If this is the case, the fields and propagation constant can be effectively modeled by those of the local fundamental mode. In a realistically non-perfectly adiabatic case, higher order modes can be excited in the taper. For a usual axisymmetric taper the fundamental LP_{01} mode can only couple to higher-order azimuthally symmetric LP_{0m} modes. The coupling will be predominantly from the fundamental to the LP_{02} mode as it is the closest higher-order azimuthally symmetric mode as seen in figure 2.4.

Up to this point, the approximative description of the optical modes as LP modes was justified as the assumption of a weakly guiding waveguide holds for most normal step-index fibers. Optical modes in a nanofiber, on the other hand, cannot be described by this approximation, because the refractive index difference between silica (core) and air (cladding) is now large in comparison. The fiber is no longer weakly guiding, and therefore the modes cannot be considered mainly transversal any more.

To describe the optical modes in a nanofiber, exact solutions of the Maxwell equations are needed. They lead to two subgroups of bound-field modes, the hybrid and transverse modes which are described in the following in the cylindrical coordinate system [15]. Hybrid modes are denoted as HE for $E_z < H_z$ and EH for $E_z > H_z$. They have six non-vanishing components of the electromagnetic field. For transverse electric (TE) modes the longitudinal component of the electric field is zero, while for transverse magnetic (TM) modes the longitudinal component of the magnetic field is zero. They have at least one vanishing component of the electromagnetic field. Considering the light ray propagation inside a fiber shown in figure 2.6 gives a more intuitive feeling for the nature of the modes. It shows a light ray spiraling in the fiber, also called a skew ray. Following the direction of the electric field vector along the ray path shows that all polarization components will be mixed during the propagation, because each component of the electric field that is perpendicular to the surface

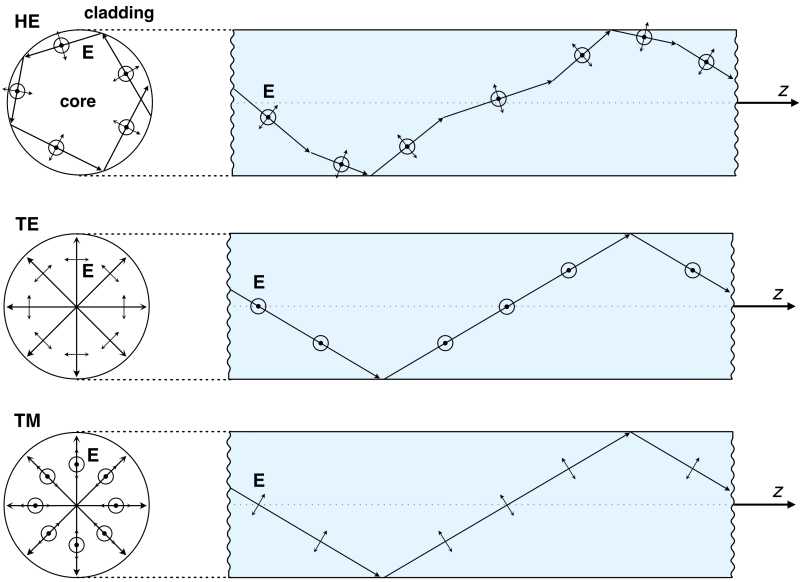

Figure 2.6: Fiber mode types that propagate in a tapered optical fiber in the light ray representation. The left shows the transverse cross-section of the fiber while on the right the longitudinal cross-section is shown. The top shows the skew rays of a hybrid mode, while the ones below show the transverse TE and TM modes. Inspired by [15, 18]

will acquire a phase shift upon reflection, whereas the parallel component will stay the same. All hybrid modes are composed of skew rays, as there are no vanishing components of the electromagnetic field [15]. In consequence, transverse TE and TM modes can only be composed of non-rotating ray trajectories in the fiber such that their polarization is not mixed after each reflection. Similarly to the LP modes, each of the exact hybrid and transverse modes can be described by the effective refractive index $n_{\text{eff}} = \beta/k_0$. The effective refractive indices of the lowest-order modes as a function of the fiber diameter are shown in figure 2.7. They increase monotonically with the fiber diameter. As in figure 2.4, $V = 2.405$ marks the boundary below which all higher order modes are no longer guided by the fiber. For arbitrary V-numbers below that, the fiber only guides the fundamental HE_{11} mode. This is an important property for designing nanofibers for their intended use.

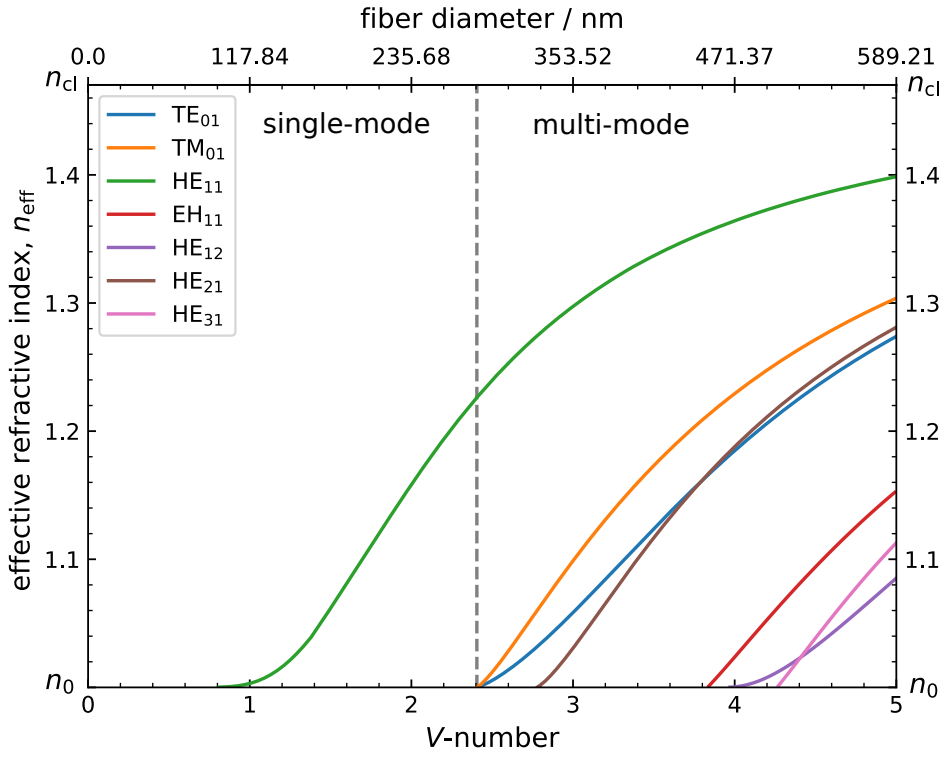

Figure 2.7: Effective refractive index as a function of the V-number for the seven lowest order hybrid and transversal modes a nanofiber can guide, the vertical line at $V = 2.405$ indicates the cutoff below which only HE_{11} can propagate

CHAPTER 3

Yb atoms coupled to super-extended nanofiber mode

In this chapter, the idea of a new experiment and its basic fundamental background are introduced that lead to the work I present in the following chapters.
A new experimental platform that combines Ytterbium Rydberg superatoms with nanofiber waveguide quantum electrodynamics is to be developed as part of a three-universities quantum physics group collaboration. This cooperation combines the expertise of the group of Arno Rauschenbeutel from the Humboldt University in Berlin on fabricating and interfacing optical nanofibers, the theoretical groundwork and expertise on Rydberg atoms and atom-light interactions of the group of Thomas Pohl from the TU Vienna and the extensive experience on Rydberg quantum optics experiments of the group of Sebastian Hofferberth from the University of Bonn.

Atoms excited to a high, metastable atomic state are called Rydberg atoms. They feature a variety of characteristics that are used in many different fields, e.g. quantum computing [27]. Due to their high polarizability [28], Rydberg atoms are very sensitive to external fields [7]. Although a Rydberg atom does not have a dipole moment without an applied field, the electric field of the charge distribution of the Rydberg electron of another Rydberg atom leads to a second-order effect of the dipole-dipole interaction, resulting in a van der Waals interaction potential $V(R) \propto C_6/R^6$ with $C_6 \propto n^{11}$ and n being the principal quantum number [7].
A phenomenon that follows from this interaction is the Rydberg blockade effect [29, 30]. The additional energy that is needed for exciting another atom to a Rydberg state because of the interaction potential can exceed the linewidth of the transitions and lasers involved, such that the excitation of a second atom is effectively prevented within a certain distance. This is also called the Rydberg blockade radius r_b. If this is applied to an atomic ensemble of N atoms for which the blockade radius of a single Rydberg excitation exceeds the dimensions of the atomic ensemble, a Rydberg superatom [7, 29] is created where the N atoms share a single Rydberg excitation. This leads to collectively enhanced Rabi oscillations, $\Omega_{\text{eff}} \propto \sqrt{N}$, which essentially means enhanced coupling of the excitation light to the ensemble.

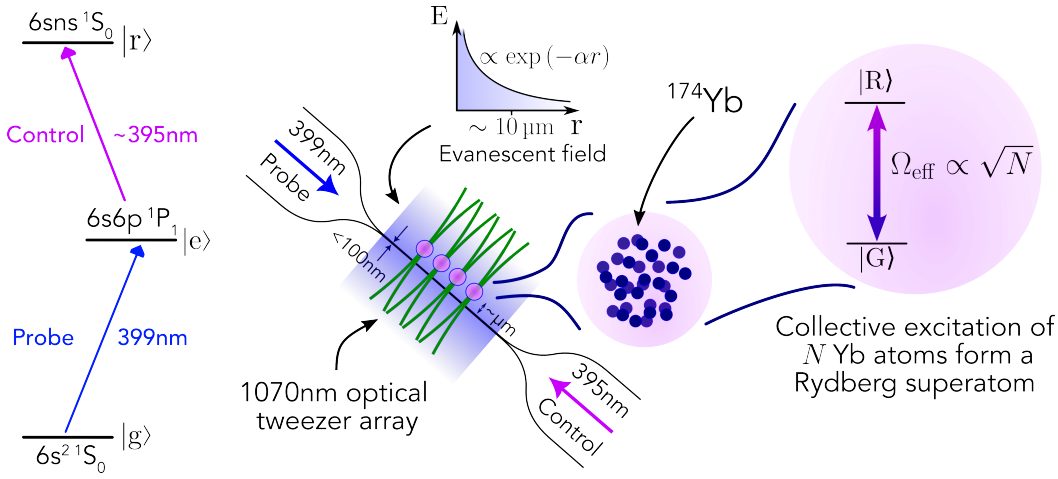

Figure 3.1: Overview of the new experimental platform. Showing clouds of ^{174}Yb atoms being trapped in a tweezer array in the super-extended evanescent field of a thin nanofiber. The 399nm and 395nm light needed for the Rydberg excitation scheme of ^{174}Yb (on the left) is guided by the nanofiber. On the right the collectivly excited cloud of N atoms is shown that form a Rydberg superatom with a collectively enhanced Rabi frequency $\Omega_{\text{eff}} \propto \sqrt{N}$. Adapted from Ludwig Müller, NQO Bonn

Combining such superatoms with nanofiber waveguides introduced in the chapter 2.2 leads to a promising experimental platform that is situated between current free-space superatom experiments [7] and nanofiber waveguide QED experiments [31–34] in terms of coupling strength and the amount of atoms that can be coupled to. The coupling strength in freespace superatom experiments is very high because of the collective coupling of an optical mode to an ensemble of atoms, but often limited to singular superatoms. In nanofiber experiments, the coupling strength is often limited due to a small mode volume that limits the amount of atoms that interact with the mode and surface interactions of the atoms that also interfere with the coherent interaction of the guided field [35].

R. Finkelstein et al. [11] proposed a solution to these limitations of current nanofiber waveguide experiments. They realized a guided optical mode with an evanescent field that extends 13λ away from the nanofiber waveguide surface, which they use for interaction with an atomic vapor. Here λ is the optical wavelength of the mode guided in the nanofiber. Figure 3.2(a) illustrates this so-called super-extended nanofiber guided field. By reducing the diameter of the waist of the nanofiber to around $0.37\lambda/n$, where n is the refractive index of the fiber core, they achieve this evanescent field extent of 13λ. Figure 3.2(b) illustrates the fiber waist diameter D dependency of the mode field diameter (MFD) of the guided mode. The MFD defines the diameter of the circular area at which it contains $1 - e^{-2}$ of the optical power of the mode [11]. As the fiber diameter decreases, the MFD follows the physical dimensions of the fiber until it diverges from this line around $nD/\lambda < 1$. From this point onward, it varies very strongly with the diameter of the waist of the fiber. It reaches an MFD of 13λ for a waist with $D = 0.37\lambda/n$ as described before, with 99.5% of the power of this super-extended mode residing in the vacuum cladding around the fiber. This realization comes close to the theoretical limit regime of tapering standard optical fibers with a fundamental mode that propagates along the taper region [36, 37].

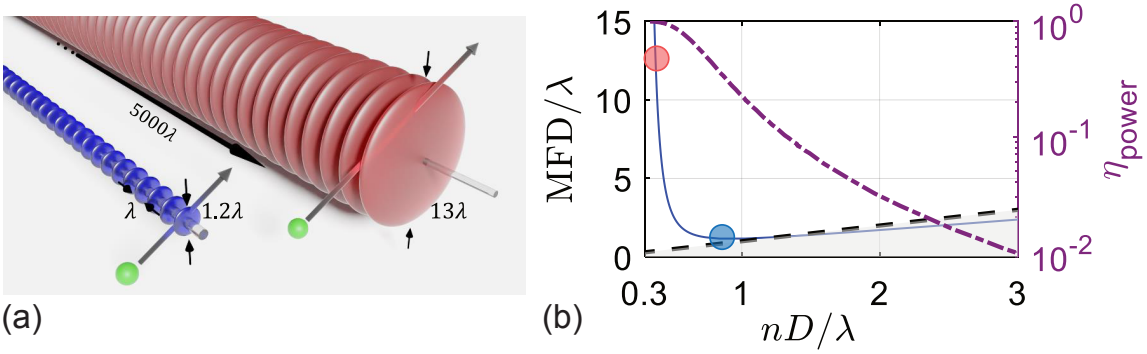

Figure 3.2: Super extended evanescent field of a nanofiber. In (a) an illustration of the thin waist region of a nanofiber is shown. On the left (fiber diameter $D = 0.9\lambda/n$), the guided mode in blue has a field diameter of MFD $= 1.2\lambda$ while on the right (fiber diameter $D = 0.37\lambda/n$), the guided mode in red has a field diameter of MFD $= 13\lambda$. Both modes are guided over a distance of 5000λ. In (b) the mode field diameter (MFD) (in units of λ) as a function of the fiber waist diameter (in units of λ/n) is shown. The dashed line shows the physical fiber dimensions from which the MFD diverges at around $nD/\lambda < 1$. The blue and red circles correspond to the guided modes in (a). The dashed purple line depicts the fraction of the power of the light residing outside the fiber. Adapted from [11]

The objective is now to combine the enhanced coupling of superatoms with the super-extended evanescent mode that these nanofiber waveguides support over an extended length [19]. The knowledge gained from the current ultracold Ytterbium 174 Rydberg quantum optics experiment of our group [38, 39] shall be introduced to the new experiment. The excitation scheme utilizes an intermediate state $|e\rangle = |6s6p\ ^1P_1\rangle$ to excite a ground state $|g\rangle = |6s^2\ ^1S_0\rangle$ ^{174}Yb atom via two-photon transition to a Rydberg state $|r\rangle = |6sns\ ^1S_0\rangle$, as illustrated in figure 3.1. A weak probe field with $\lambda_P = 399$nm drives the transition $|g\rangle \rightarrow |e\rangle$ and a strong control field the transition $|e\rangle \rightarrow |r\rangle$ with $\lambda_C \approx 395$nm.

Figure 3.1 brings all these concepts together and illustrates the new planned experimental platform in which an ultra thin nanofiber is used as a waveguide for guiding Rydberg excitation light of 399nm and 395nm to couple to clouds of ^{174}Yb atoms, via the emerging super-extended evanescent field [11]. The atom clouds are trapped in an optical tweezer array along the waist of the nanofiber to effectively create multiple superatoms by the collective excitation of the respective atom cloud. To achieve such a super-extended evanescent mode field diameter of $13\lambda \approx 5.2\,\mu$m the waist of nanofiber needs to have a diameter of $D = 0.37\lambda/n \approx 100$ nm for the probe field wavelength of $\lambda_P = 399$ nm and a refractive index of $n = 1.47$ for SiO_2 at 399 nm. These nanofibers are fabricated by our collaborators from Berlin.

Because our group has limited experience with nanofibers, an essential part of implementing and developing this new experimental platform is to construct and set up the necessary infrastructure to enable dust-free handling of such fibers. In addition, it is unknown how the nanofibers behave under the targeted propagation wavelengths of 399nm and 395nm. Therefore, the goal of this thesis is to construct and establish a working space in which nanofibers can be safely handled without dust contamination, brought into a vacuum environment, and evaluated for their transmission behavior.

CHAPTER 4

Nanofiber testing setup

The nanofibers are very sensitive to dust particles and air flow. Due to the increased requirements for a dust-free working area, we designed and built a dedicated testing setup to characterize our nanofibers. The description of the setup is divided into five topics: testing table construction, clean air setup, vacuum chamber, optical setup, and data acquisition. I took over the construction of the setup in an early stage where only the testing table frame was built, the optical breadboard was installed. All of the additional components were built and installed by me.

4.1 Testing table

The testing table is a self-built construction of aluminum profiles and wood panels. An optical breadboard (750 mm x 1200 mm x 60 mm) from Thorlabs is installed to mount the optical setup and is used as a workspace. Sorbothane sheet cutouts are installed underneath the optical breadboard at all contact points between the optical breadboard and the frame to dampen vibrations that could disturb the optical setup. A flow box module, a separate clean air box, and a vacuum chamber are installed in conjunction with an optical setup to test the nanofibers under clean air and vacuum conditions. The setup is designed to make fiber testing an easily repeatable process, while also gaining experience for the group on how to handle such fibers without contaminating them, which would lead to permanent damage. It is self-contained and separate from the current Yb experiment [38, 39] in our group, so it does not rely on any other system other than the blue 399 nm light coming from one of the experimental tables through an optical fiber. Storage shelves above the flow box and below the optical breadboard give space for power supplies, vacuum prepump, and all the necessary fiber preparation-related equipment. The power sockets are strictly separated to reduce possible sources of noise and interference for the measurement electronics. The table also features a switchable LED light source as a working light on the table and a power distribution box for our modified biased Thorlabs photodiodes for use with an external power supply instead of batteries. To block laser light going off the optical table black laser proof plexiglass sheets are installed all around the optical table that can be slid open or shut. They also provide physical protection against dust from outside the table.

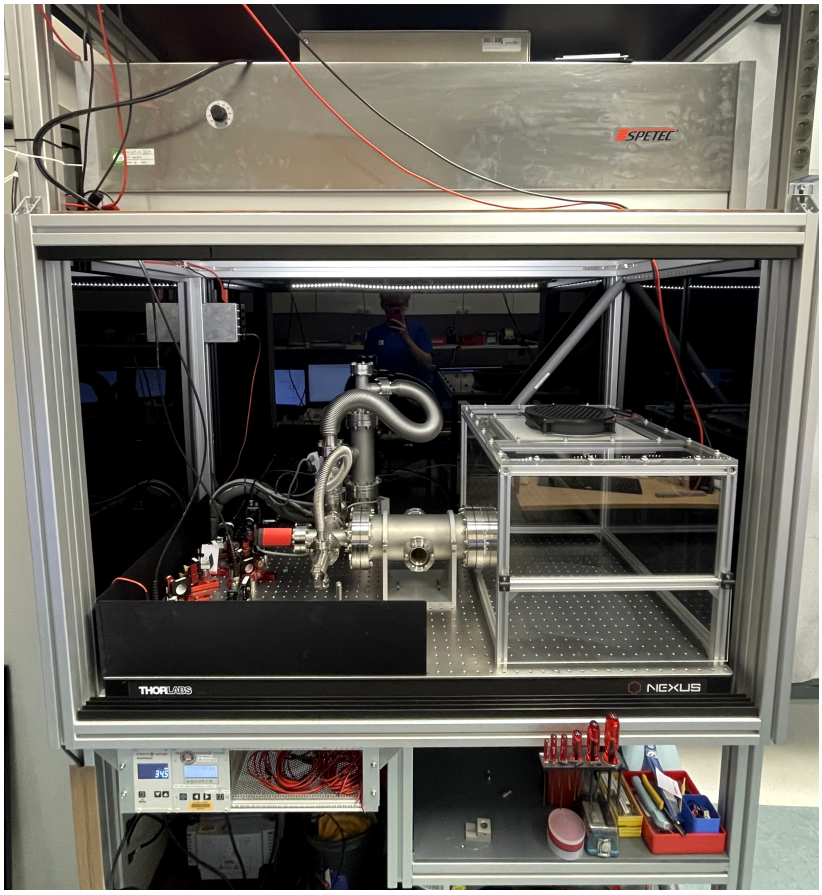

Figure 4.1: Fiber testing table construction from aluminium profiles with a mounted optical breadboard. It consists of a flow box module on top, an inner clean air box on the right with a hatch for working, a vacuum chamber with viewports and a two-stage evacuation system in the middle. On the left, covered by laser blocking plates is an optical setup for transmission analysis of coupled optical fibers.

4.2 Clean air setup

Because nanofibers are extremely sensitive to dust contamination in a sense that dust particles can burn onto the fiber and consequently permanently reduce transmission. Therefore, the table was designed with a dust-free setup in mind. As a basis, a laminar flow box module, Spetec FMS 75 Basic, is installed on top of the table to supply the optical table with high-efficiency particulate air (HEPA) H14 filtered dust-free air. An inner clean air box is used as a separate enclosure to work with the nanofibers in filtered HEPA H14 dust-free air again with reduced airflow to protect the fibers even more. It is shown in figure 4.2. This box is also used to install the nanofibers in the vacuum chamber. It is self-built and constructed from aluminum profiles and acrylic sheets. Every connected part is sealed using adhesive foam around all edges of the acrylic sheets, the aluminum frame, and the HEPA 14 filter inside the box. The top sheet is attached using screws and plastic washers, which are intended to protect the acrylic sheet from stress fractures. A large fan is mounted on top of the box to push air through the underlying filter. As I detected a backflow of air beside the fins of the fan

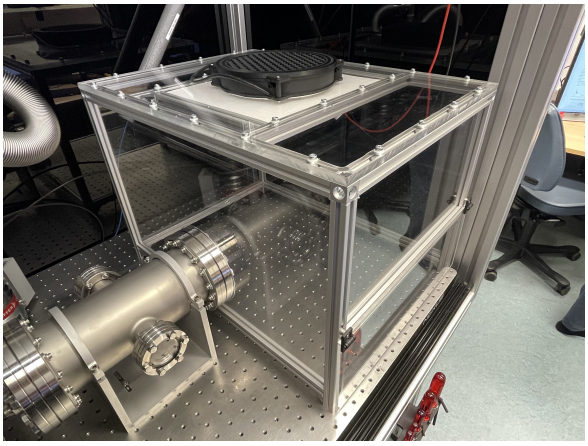

Figure 4.2: Clean air box built from plexiglass and aluminium profiles with dust-proof sealed edges. A hatch in front opens up the workspace. On top a fan and a HEPA 14 filter are installed.

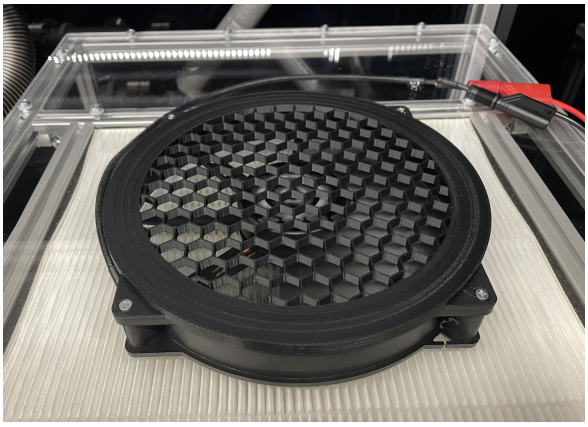

Figure 4.3: 3D printed fan faceplate to redirect the backward flow of air, it also acts as a fingerguard.

and in consequence an unnoticeable airflow inside the box, a custom faceplate to guide the airflow is designed and 3D printed. This reduces the intake area, blocks the backward outflow, and serves as a fingerguard to protect the fan itself and the operator's fingers. It is depicted in figure 4.3. With the faceplate in place the outflow is minimized and the airflow inside the box is increased to a sensible level where one achieves a laminar flow that is high enough to provide a dust free area, but low enough to not break the fibers on its highest speed setting. A hatch for working with the fiber inside the box is installed on the front of the box, as well as an opening for accessing the vacuum chamber.

I evaluated the air cleanliness in the setup using a borrowed particle sensor setup. It consists of two Sensirion SEN54 particle sensor modules that are factory calibrated and were also referenced to a handheld high-accuracy particle sensor from the clean room facility associated with the university. I concluded that the air-filter setup we use meets its specifications, with only five dust particle events being measured inside the clean air box in a timeframe of 6 hours. Therefore, this setup is sufficiently clean for handling nanofibers according to our collaborators from Berlin.

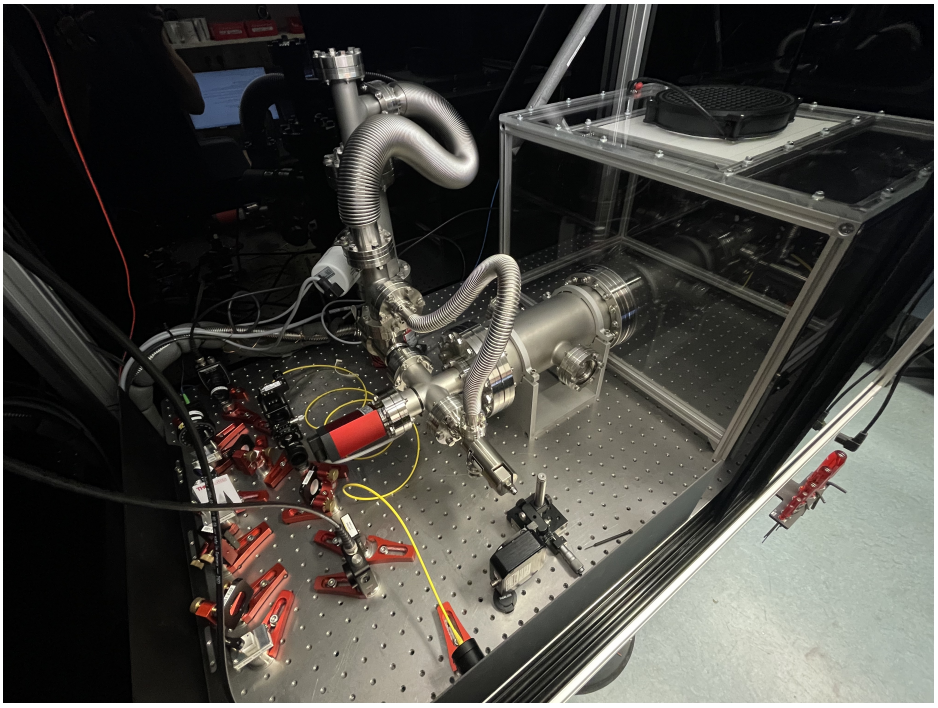

Figure 4.4: Vacuum chamber with attached two stage evacuation system with a needle valve for slow and controlled evacuation. A big corner valve in the back used for faster evacuation in the lower hectopascal regime. Viewports on the front and the back of the chamber provide optical acess of the nanofiber inside. The right side is accessible from inside a clean air-box.

4.3 Vacuum chamber

The nanofiber testing vacuum chamber was designed with optimal accessibility and visibility of the nanofiber in the chamber in mind to be able to gather as much information as possible while testing the fibers. It can be seen in figure 4.4.
It consists of a single cross-part with two axes, one with a CF100 and the other with a CF40 flange. Windows are installed to observe the nanofiber inside the chamber on the front and back CF40 flange. On the left a 4 way CF40 cross flange connects the chamber with a Pfeiffer PKR 360 full range gauge, a full metal CF40 corner valve, and a Vacgen CF16 needle valve. The Vacgen CF16 needle valve is connected to a CF40 T-piece via a CF16 vacuum bellow which bypasses the full metal CF40 corner valve as the CF40 T-piece is connected to the Pfeiffer Vacuum HIPACE 80 turbo pump via a CF40 vacuum bellow. This combination essentially functions as a two-stage vacuum setup. The needle valve is used between 1 000 hPa and 1 hPa to evacuate the chamber at a slow rate to prevent a too high flow rate that could break the nanofiber apart or churn up residual dust from inside the chamber that could settle on the nanofiber. Below 1 hPa, the large corner valve can be opened in addition to continuing to evacuate the chamber.
A Pfeiffer Vacuum MVP 040-2 diaphragm pump and a Pfeiffer Vacuum HIPACE 80 turbo pump are used for vacuum chamber evacuation. The diaphragm pump is used as a pre-pump for the turbo pump. It needs to be running well before starting the turbo pump to bring down the pressure from ambient to the low hectopascal regime.

On the right, the testing vacuum chamber reaches into the inner clean air box where a Swagelok feedthrough and a nanofiber holder mounted on the flange are installed to guide the fiber into the vacuum chamber.

4.3.1 Evacuation procedure

The basic start-up procedure consists of completely closing the large CF40 corner valve and the needle valve, starting the prepump, and waiting until the pressure on the turbo pump gauge is in the range of 1 hPa. Afterwards, the needle valve is opened ever so slightly so that the measured pressure at the pump gauge rises only by up to 0.3 hPa. This ensures a slow evacuation speed to protect the fiber from residual dust, as described previously. The opening of the needle valve is adjusted according to the current pressure to maintain a slowly increasing pressure gradient. The goal is to go from 1 bar to 1 mbar. I determined 2-4 hours to be a good time frame to aim for, with the pressure gradient being the shallowest with 2 hPa min^{-1} to 5 hPa min^{-1} at the beginning. After reaching the 1 hPa regime inside the vacuum chamber, the turbo pump is activated. As the turbo pump spins up and the pressure outside the chamber drops to 1×10^{-5} hPa the needle valve and the corner valve can be opened up further until they are fully open. The pressure level is low enough so that the risk of unsettling residual dust in the chamber is mitigated.

After 4 days of evacuation, the lowest pressure of 8.64×10^{-8} hPa can be achieved inside the chamber. That is the same order of magnitude where the vacuum starts being referred to as ultra-high vacuum (UHV), but it does not go lower than that. Closed valves lead to an increase in chamber pressure, but to a stabilization at 1×10^{-7} hPa to 5×10^{-7} hPa. This rise in pressure can be explained by the outgassing of the epoxy glue on the nanofiber holder and other organics still inside the chamber. As the chamber is not baked, this is probably the lowest achievable pressure with this setup in its current state. For the experiment itself, baking the experimental chamber and additionally using an ion pump is a necessity to reach UHV levels.

4.3.2 Fiber feedthrough

There are different methods to get a fiber into and out of the vacuum chamber and still maintain UHV levels. As mentioned already mentioned, a Swagelok solution with an inserted Teflon two-way fiber cone is used for this setup.
The conus has two small holes next to each other so that a fiber can enter on one hole and exit the chamber through the other hole again. With the fibers inserted the nut gets closed, the teflon conus gets compressed into the fitting, and consequently the fibers are squeezed to make it airtight [40]. A clean vacuum assembly procedure is of course a must for the fiber feedthrough assembly due to its tight tolerances.

Other solutions discussed, which may be applied for the main experiment when the testing phase is over, include gluing the fiber to a perforated flange with vacuum-proof epoxy glue. This has a lower error rate in the sense that the teflon seal might not work sufficiently every time, a lower compression strain on the fiber, and high vacuum compatibility. However, the flange needs to be exchanged as a whole every time the fiber needs to be exchanged in comparison to only a small teflon conus with the current solution.

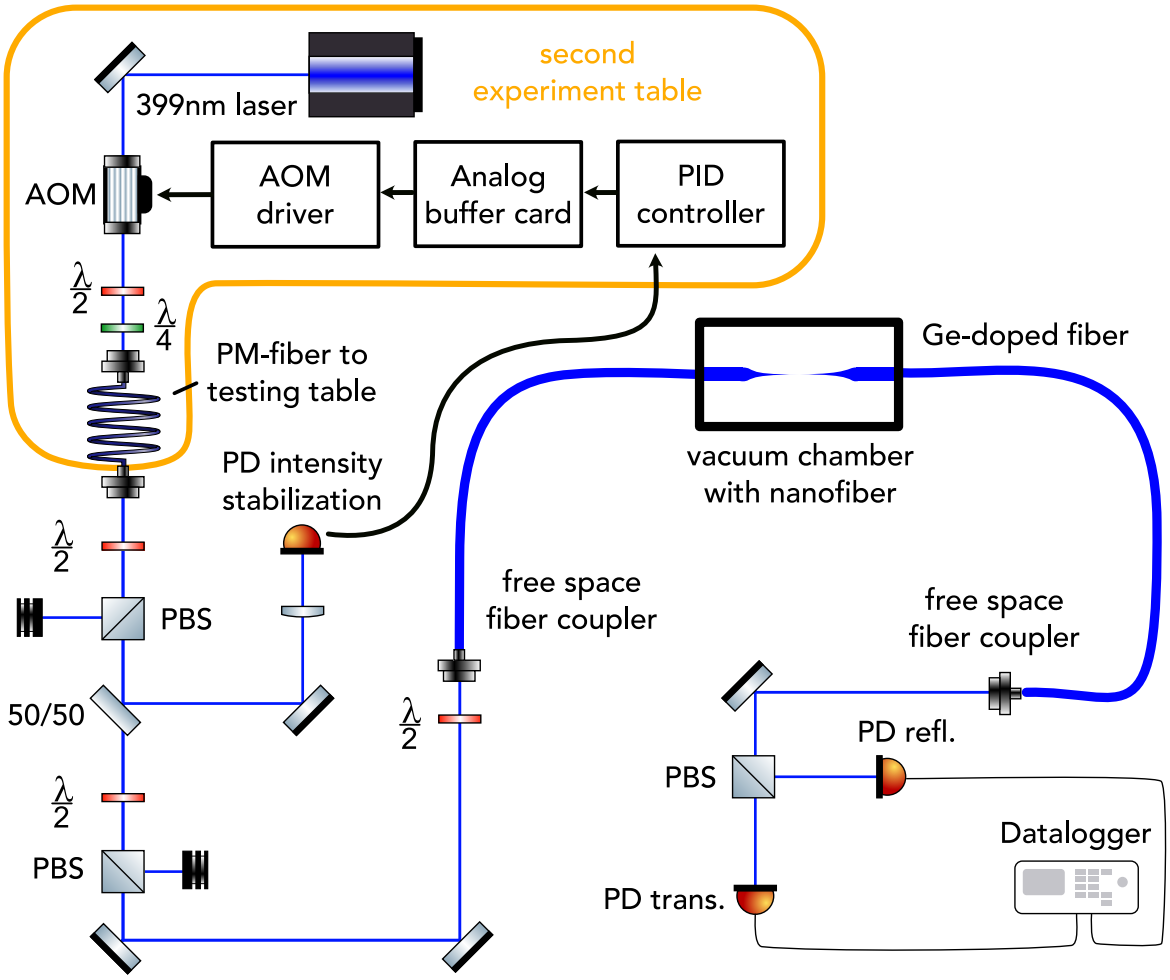

Figure 4.6: Illustration of the complete optical setup on the fiber testing table for transmission and polarization analysis of the nanofibers. The box in orange marks the parts that are not on the table.

The currently used solution is the best for the testing setup due to time and cost efficiency, as the fibers are exchanged more often, but might not be the best for the future experiment where UHV levels need to be reached.

4.4 Optical setup

The optical setup on the testing table has a small footprint, as the usable space is constrained by the vacuum chamber and the clean air box beside it on the same table. The whole setup is depicted in figure 4.6.

We are working with a 399 nm laser light source on the testing table which orginates from a 10 m long polarization maintaining single mode Thorlabs fiber (P3-405BPM-FC-10) going to the second experiment table. On this second table, 399 nm light from an unused laser arm is coupled into the fiber.

The laser light comes from a Toptica TA-SHG 399 nm laser, which is a high-power, tunable, frequency doubled diode laser named "Obelix". In the beampath in between the laser and the fiber incoupler a Gooch and Housego IM-110-2C10BB-3-GH27 acousto optical modulator (AOM) is installed and adjusted to have its highest intensity in the $m = -1$ diffraction mode so that it can be used to stabilize the intensity of the beam after the fiber on the testing table by modulating the AOM diffraction power accordingly. Two mirrors are installed after the AOM to couple light into the fiber. In addition, two $\lambda/2$ plates are installed in the beam path directly in front of the fiber incoupler to control and adjust the polarization of the beam.

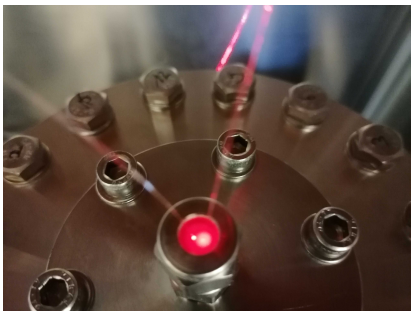

Figure 4.5: Vacuum fiber feedthrough of the vacuum chamber with installed fiber glowing red by using a fiber testing pen.

The fiber coupling setup, depicted in figure 4.7, consists of a Thorlabs Z-Axis Translation Mount (SM1ZA) in a cage setup with a Thorlabs molded glass aspheric lens in front that needs to be matched to the NA and MFD of the fiber used and the diameter of the to be incoupled beam.
This setup is also the recommended solution from our collaborators from Berlin as it gives a very precise adjustment of the lens position to optimally focus the beam onto the fiber facet.

On the testing table, we have a basic fiber outcoupler with an adjusted $f = 15.29$ mm aspherical lens to collimate the beam. A $\lambda/2$ plate and a polarizing beam splitter (PBS) in transmission are used to have stable polarization after the fiber. The reflected light of a 50/50 beam sampler, placed in transmission after the PBS, is focused onto a Thorlabs DET36A2 biased photodiode to pick up the light for the intensity stabilization of the beam. In transmission after the 50/50 beam sampler, another $\lambda/2$ plate and a PBS. By rotating the $\lambda/2$ plate, the ratio between reflected and transmitted light can be changed. The reflected beam is directed into a beam dump.
In transmission after the PBS are two mirrors for coupling the beam into the nanofiber. The coupling setup is again a Thorlabs Z-Axis Translation Mount (SM1ZA) in a cage setup with a Thorlabs molded glass aspheric lens in front. Another $\lambda/2$ plate directly in front of the coupler is used to rotate the polarization for polarization stability measurements after the fiber.

At the other end of the fiber there is a basic fiber coupler with another molded glass aspheric lens to collimate the beam. Another PBS is used after the outcoupler to separate the s- and p-components of the light and measure the intensity of each as the reflected and transmitted light, respectively, with Thorlabs DET36A2 biased photodiodes. Their signals are recorded with a PicoLog ADC-20 data logger.

4.4.1 Intensity fluctuations on the testing table

When evaluating the optical setup I noticed substantial relative intensity fluctuations of up to 5.5% of the beam coming out of the 10 m polarization maintaining (PM) fiber onto the testing table. The beam in front of the fiber does not show these fluctuations and is very stable with only 0.4% of relative deviations of the signal. These observations are depicted in figure 4.8. A spectral analysis of the time series shows mainly low frequency components below 5 Hz.

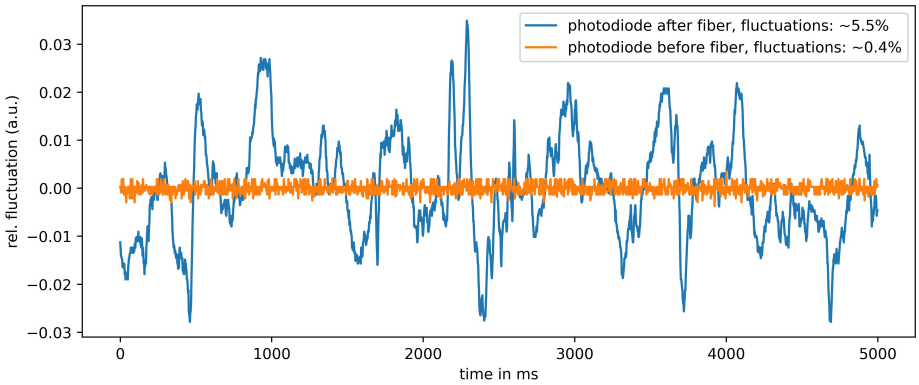

Figure 4.8: Intensity fluctuations over time in front of and after the fiber in comparison. Depicted as the relative fluctuation around the normalised signal.

Investigating this problem leads to multiple possible sources for these fluctuations. Reflections on the faces of the fiber ends can be ruled out mainly because both ends have an angled tip, leading to an optical return loss of > 60 db. The propagation of the cladding mode is also unlikely to be the main cause, because the cladding modes get attenuated quite quickly and are mostly a problem of shorter fibers in the lower than 2 m range. To exclude mode hopping of the laser, the alignment mirrors of the cavity were systematically misaligned, but no correlation between the cavity alignment and the fluctuations could be found. The amplitude and shape of the intensity fluctuations do not change.

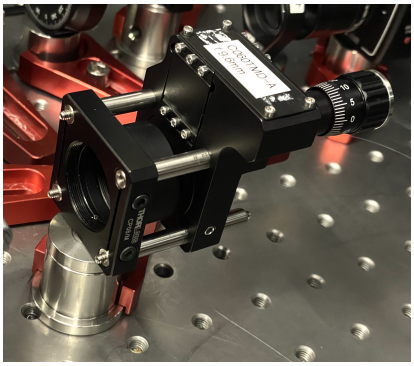

Figure 4.7: Fiber coupling stage with z-axis fiber adjustment

However, observing the beam from the laser with a beam camera behind a lens with a large focal length of $f = 750$ mm in the far field showed pointing stability issues of the laser. Due to the observed nature of the beam-pointing instability the coupling efficiency can vary on the observed intensity fluctuations timescale, which would explain the observed fluctuations. We concluded that the pointing instability might have the biggest influence on the intensity fluctuations. As an intensity stabilization is wanted anyway, further investigations on the pointing instability is of no great concern for the time being. The observed fluctuations in this low frequency regime should be compensated for by the intensity stabilization. Other effects like thermal drifts should also be mitigated by a intensity stabilization as they do happen on an even larger timescale.

4.4.2 Intensity stabilization

As described before, an intensity stabilization is set up for the testing table laser beam. In figure 4.6 all the components involved can be seen. The principle is to have a laser beam that gets diffracted by

Figure 4.9: Proportional–integral–derivative (PID) controller built by the electronics workshop of the group and modified by me. The PCB in the bottom shows the modifications. The inputs and potentiometer on the front panel are relabled for their modified use.

an AOM in the first order coupled into a polarization-maintaining single-mode fiber. After the fiber a $\lambda/2$ plate and a PBS are placed such that the polarization is well known and fixed. A photodiode that monitors the intensity is right behind the polarization filter, picking of the signal with a 50/50 beam splitter. The AOM is used to vary the amount of light that is diffracted into the 1st order mode on much faster timescale than the intensity fluctuations itself. It is used to counteract the intensity drifts or fluctuations. This is done by active stabilization using a feedback loop. It regulates the RF power that is applied to the AOM such that the signal on the photodiode stays at a constant level. The Thorlabs DET36A2 biased photodiode signal goes to the first input of one of our self-built proportional–integral–derivative (PID) controllers. This PID controller board is depicted in figure 4.9.

As the first stage of the PID controller sums the signal of input 1 and the inverted signal of input 2 which gives $V_{out} = V_1 + (-V_2)$, so it effectively acts as a subtraction stage. On input 2 a reference voltage is set. In this case, the reference signal is set on the PID controller itself, by a modification of circuit I applied.
The first stage therefore effectively creates an error signal that tells the circuit how much the current intensity differs from the setpoint. In this case, only the P and I circuits of the board are used. The P circuit gives a proportional response to the magnitude of the error signal. The ratio of the output response to the error signal is determined by the set proportional gain K_p. Increasing the proportional gain generally leads to a decreased system response time, but if it is too large, the system will start to oscillate and it may become unstable and oscillate out of control. To obtain an ideal response, the gain needs to be accurately adjusted to the response characteristics of the system at hand. The I circuit integrates the values of the error signal over time, with the result that the integral response continuously increases as long as the error signal is not zero. This effectively drives the steady-state error to zero. The amount of action it has on the output signal is determined by the integral coefficient K_i, which also needs to be tuned to the overall response of the system to make it as effective as possible without having too much of an overshoot. In most cases the D circuit which is a derivative response is not needed for this type of intensity stabilizations, so we dont go into detail here.

As mentioned before the PID controller board got modified from the stock functionality. As the scan input is unused in this case, the scan gain potentiometer is rewired to act as a simple voltage divider by connecting it to the +15V power linear power supply on the board and GND pin. The signal output pin is connected to input 2 by a green cable to the unpopulated R43 pad, which is connected to the input pin 2. This then acts as an internal reference voltage without needing an additional external source. In the lower part of figure 4.9 these modifications are depicted.
The input 2 BNC connector is now used only for monitoring as long as the internal three pin connector is connected to the power supply pins. If its disconnected it can be used as a normal reference voltage input as before. The scan potentiometer now acts as a reference voltage potentiometer which adjusts the voltage going into input 2 between 0V and +15V. The PID controller is installed next to an analog buffer card in a rack above the Obelix laser. The analog buffer card is used to shift the feedback voltage range of the PID output from -12V to 12V to the analog input range of the AOM driver box that is connected to the AOM which is 0V to 10V.

The feedback loop must be tuned to the response of the system. Therefore, a triangle wave from 0V to 10V at 10Hz gets fed into input 2 instead of a constant voltage, and the photodiode signal, the error signal, the PID output and the triangle wave are monitored on an oscilloscope. Only the P part is then

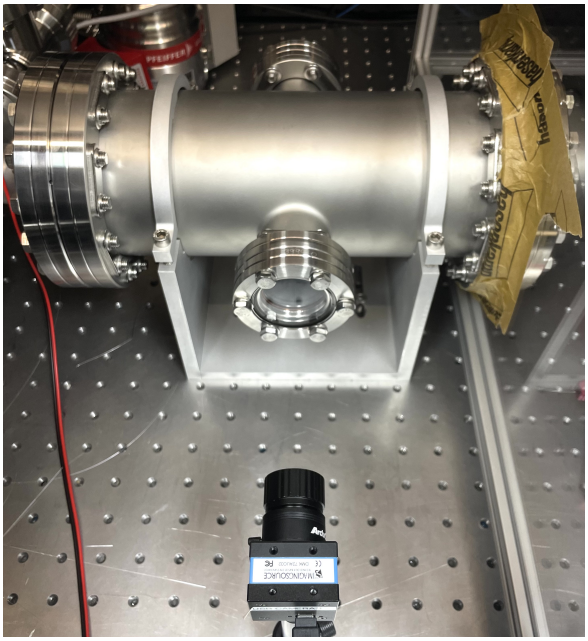

Figure 4.10: Imaging Source monochrome DFK 72AUC02 CCD camera with a $f = 25\,\text{mm}$ lens pointed onto the vacuum chamber viewport to observe the installed nanofiber.

activated and the gain is adjusted so that the photodiode signal follows the triangle wave reference signal. Afterwards the I part is also activated and adjusted that the photodiode signal follows the reference even more closely.

Then a square wave is applied as a reference signal with an offset moving in to the middle and an amplitude smaller than the full range of the AOM driver box. With this signal applied P and I can be further optimized such that the rise and fall times are minimized together with an overshoot of ideally less than 5%. Using this optimized feedback loop yields a much more stable intensity on the fiber testing table with a relative fluctuation of 0.27% (4.0mV/1.5V). The intensity stabilization mitigates the problems described in section 4.4.1 to a high degree. With this level of stability the main measurements can be performed accurately.

4.5 Data acquisition

In this section, the measurement setup is discussed. A Rigol DS2102E two channel 100MHz oscilloscope quickly became insufficient as the need for longer measurement runs and multi channel monitoring arose. An eight channel PicoLog ADC-20 datalogger is installed in the setup and positioned on top of the shelves of the table in addition to the oscilloscope. To accompany the datalogger, a computer with a movable and tiltable screen is also installed to be used as a separate working environment. It runs all the necessary software to evaluate and save the data measured by the datalogger.

To observe the waist and taper region of the nanofiber while light is coupled into the fiber, an Imaging

Source monochrome DFK 72AUC02 CCD camera with a $f = 25\,\text{mm}$ lens is used. The camera is mounted on a post and is pointed towards the front window of the vacuum chamber, from which the nanofiber on its holder can be observed. The camera software is used to capture images in specific time intervals to correlate changes in transmission and polarization with changes in the observed nanofiber. As the camera settings can be fully configured by the software, the exposure can be specifically chosen and fixed, such that intensity changes can also be observed in the camera picture.

CHAPTER 5

Fiber testing

In this chapter the process from the selection of an optical fiber suitable for the project, the further processing of the fiber, the testing of the nanofibers and the fiber material itself is described and explained.

5.1 Fiber selection

One goal of the project is to find an optical fiber that is suitable for the transmission of 395 and 399 nm light and can be pulled into a nanofiber by our collaboration partners from Berlin. A waist diameter of 100 nm should be reached. The state of the art is to pull Ge-core-doped optical fibers into nanofibers, but for wavelengths different from the ones needed for this project. This involved a market research as Ge core-doped optical fibers for 395 nm and 399 nm light are not so common in the optical fiber industry. The specified cutoff wavelength is often right in this region with an uncertainty (370 ± 20) nm that is too close to 395 nm to be usable without concern. Most companies only offer pure silica core optical fibers with flourine-doped (F-doped) cladding for these wavelengths and below due to the effects of photodarkening or so called solarization [41], which is a process that increases the attenuation of the signal over time.

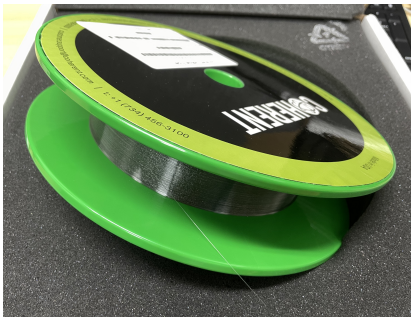

Figure 5.1: Bare Coherent 405-HP fiber on a fiber spool

Coherent was the only manufacturer to sell an optical fiber with a germanium-doped core and a uniform silica cladding designed for 400-550 nm with a selectable cutoff wavelength, called 405-HP. They do this by testing and measuring batches after production to classify and guarantee a certain cutoff wavelength. However, they do not have or provide any data on photodarkening. As this was the only suitable prospect, a 381 m spool with a measured cutoff at 370 nm was bought, as this fits the project's requirements quite well. Another 110 m spool with a cutoff at 390 nm was bought a few months later for further testing purposes of the fiber material. Both have a 2.1μm Ge-doped core and a 125μm uniform silica cladding inside a 250μm acrylate coating.

5.2 Fiber termination

The optical fibers on the spools are bare, so there is no additional protective sleeve or connectors. This means that full customizability is possible depending on the needs. Initially, the proposed solution from Berlin is tried. This means terminating the fibers with a temporary bare fiber terminator and leaving the fiber unprotected without a sleeving. A Thorlabs BFT1 bare fiber terminator is used in combination with a Thorlabs B30126C3 FC/PC connector with a ceramic ferrule. Figure 5.2 shows such a fiber terminator. To terminate the fiber, a piece is cut off from the spool with the desired length of the fiber. On both ends, the acrylate coating is removed with a certain fiber stripping tool chosen for the fiber dimensions. It mechanically removes the coating in one step. Other solutions for fiber stripping are to thermally remove the coating by heating it up to the melting point of the acrylate, or to chemically dissolve the coating with heated sulfuric acid or paint stripper [42]. Chemical removal of the coating being the best option when high precision and reliability is needed. As this process is unpractical for a lot of repeated fiber tests, mechanical stripping is sufficient as it is one of the fastest procedures and still highly reliable if done correctly. For the final experiment, the other stripping procedures may be considered to achieve the highest level of reliability.

Figure 5.2: Temporary bare fiber terminator

Figure 5.3: Mechanical fiber coating stripper and a fiber scoring pen

After stripping the fiber by about four to five centimeters, the residual acrylate debris is cleaned off by using a lint free lens tissue that is soaked in isopropyl alcohol (IPA or 2-propanol). The fiber end is pressed firmly between the fingers inside the folded tissue and gets pulled out of it, cleaning the fiber surface. Subsequently, the fiber is inserted into the bare fiber terminator through the ferrule until it sticks out by about two centimeters. Now a mechanical cleaver or a scribe pen gets used to cleave the end of the fiber. Such a scribe pen and a mechanical coating stripper are shown in figure 5.3. After cleaving, the fiber is recessed until it is flush with the ceramic ferrule.

The scribe pen is the recommended tool for cleaving, as it produces less fiber waste than the mechanical cleaver, which requires a longer protruding fiber from the fiber terminator to work properly. It also produces the same to even higher quality cleave results if done by a skilled person than the basic mechanical cleavers from Fujikura. High quality in this case means a clean, uniform fiber facet without scratches or chips and a cleave angle lower than 0.5° to avoid high insertion loss levels. The difference in quality of both techniques was determined by ten subsequent cleaves with each system which were evaluated with a fiber microscope for surface quality and a checked with the Fujikura 90S + splicer [43] for the lowest cleaving angle. The tests resulted in a subjectively similar quality surface and an objectively slightly better mean cleave angle of $(0.3 \pm 0.1)^\circ$ for the scribe pen versus $(0.5 \pm 0.1)^\circ$ for the Fujikura CT50 cleaver. This shows that both solutions are equally usable. In this

case, the scribe pen is favored to be able to work with much shorter fiber pieces.

To make a good cleave with the scribe pen the protruding fiber needs to be scored. This means that the ruby blade of the scribe pen is used to create a small scratch on the fiber. The pen should be held perpendicular to the fiber to ensure correct scoring. The fiber then needs to be pulled along the mechanical axis of the fiber so that the stress from the scoring leads to a shock wave through the material to obtain a clean cleave perpendicular to the fiber. Pulling the fiber apart is done by hand, which is why it is crucial to have experience performing this procedure. Any torsion applied while pulling leads to an angled cleave which is undesirable. The quality of the scoring can be assessed during the pulling procedure by sensing if the required pulling force is higher than that needed for a clean cleave.

The cleaved and recessed fiber is observed with a fiber microscope to check on the cleave quality. On both sides of the fiber a temporary connector is installed using this method. To test the fiber, it is connected to the fiber coupler setup in the optical setup on the fiber testing table described in section 4.4. The coupling efficiency should be maximized to make sure that the beam is optimally focused on the core of the fiber and that as much light as possible is coupled into the fiber. The efficiency is measured by the quotient of the light intensity in front of the fiber and the intensity coming out of the fiber at the other end. As the electric field that is guided inside a single mode fiber can be approximated sufficiently by a Gaussian intensity distribution, the outgoing beam of the fiber can be described by a Gaussian beam with the beam waist at the fiber tip [15]. This means that if the incoming beam can be mode matched with the fiber mode so that they are equivalent, the theoretical coupling efficiency would reach 100%. The theoretical coupling efficiency can be calculated by the overlap of the two modes. Every deviation from an ideal Gaussian beam leads to a reduced coupling efficiency. A mismatch in the spot sizes, shifts, or tilts of the modes with respect to each other and optical aberrations or diffraction in the optical system are examples which lead to deviations from an ideal Gaussian beam. To match the fiber mode with the 399 nm light setup on the fiber testing table, the mode field diameter (MFD) needs to be known. With the MFD the required incident beam parameters can be calculated using Gaussian beam propagation. The MFD is constant along the fiber length and is the width of the mode at which the intensity is down to e^{-2} times the peak intensity.

5.2.1 MFD measurement

In general, the MFD can be measured in the near-field directly at the tip of the fiber using an imaging microscope lens with the focal plane at the tip of the fiber. The value of this technique is questionable for MFDs under 10μm as the positioning accuracy and diffraction-limited resolution of the lens become comparable to the MFD without even taking the typical point-spread function of microscope lenses into account.

This is why the MFD is often measured using the far-field. One of the methods is performed as follows. The bare fiber output with no lens in front of it of a fiber on the fiber testing table with 399 nm light coupled into it is pointed perpendicular onto the sensor of a beam profiler camera. The beam profiler camera is mounted on an x-y micrometer stage to accurately adjust the distance z between the fiber tip and the camera sensor. With this setup, the beam radius $w(z)$ is measured with the beam profiler camera for 25 different distances from the fiber. By fitting the measured data linearly and taking the

slope $m = w(z)/z$ of the fit, the divergence angle

$$\theta = \lim_{z \to \infty} \arctan(w(z)/z) \tag{5.1}$$

is obtained. Inserting the calculated divergence angle into a rearranged formula for the divergence angle in the far field yields the beam waist

$$w_0 = \frac{\lambda}{\pi\theta} \tag{5.2}$$

The MFD is then just MFD = $2w_0$. Using the obtained MFD the required focal length f of the lens to focus the collimated beam to the needed spot size that resembles the MFD can be calculated by using any Gaussian beam propagtion tool. This measurement results in a slope of $m = (0.1509 \pm 0.0004)$ and therefore in a mode field diameter of MFD = (1.696 ± 0.003) µm at 399 nm for the Coherent 405-HP fiber. For a beam diameter of (2.01 ± 0.04) mm the most suitable focal length of the available lenses was determined to be $f = 6.2$ mm. However, the best coupling efficiency achievable by using this focal length with this fiber in the optical setup on the fiber testing table was only (29.3 ± 0.2) %. Further testing with different focal lengths did not yield higher coupling efficiencies.

5.2.2 Permanent fiber termination

Due to the low achievable coupling efficiency and having intensity fluctuations after the bare fiber piece, a different approach for fiber termination is tested. These fluctuations after the Coherent test fiber on the table of up to 4% relative to the signal were occuring although the installed intensity stabilization was fully working. Beam pointing on the table could be excluded, so the fiber termination was a possible source of these new fluctuations.

Commercially available fiber optic patch cables come in different packaging compared to the bare fiber currently in use for testing. The bare fibers are sleeved by a plastic or metal tubing and have fixed connectors on both sides of the fiber. The tubing protects it from influences from the outside, makes them more rigid, and therefore making it less prone to being bent until its point of failure. Despite having slightly better isolation from temperature drifts, tubing does not provide any other optical or mechanical stability advantages. Connectors instead can provide this because the fiber is glued to the ferrule instead of being only pushed into it and clamped to not move. The fiber tip is also not cleaved, but polished. An angled fiber tip is also possible this way to prevent back reflections on the fiber endface. To test whether this actually provides a higher level of mechanical stability of the fiber tip leading to higher coupling efficiency and lower intensity fluctuations after the fiber, connectors of different kinds (FC-PC and FC-APC) with ceramic ferrules, tubing material, strain relief boots, suitable epoxy glue (Thorlabs F120 and F112), and polishing sheets are bought.

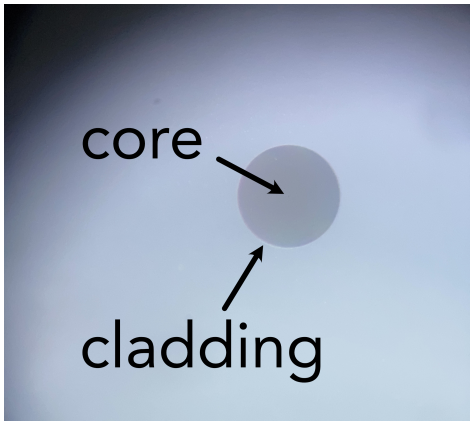

Figure 5.4: Polished fiber facet viewed under the fiber microscope with core and cladding indicated

For the process of connectorizing and polishing the bare fibers, a Thorlabs guide [44] is followed. Therefore, a detailed description of this process is omitted, and only a rough idea is given in the following.

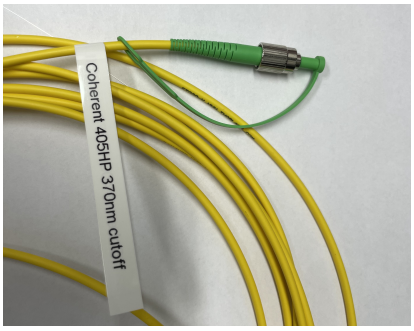

Figure 5.5: Coherent 405HP fiber permanently terminated and sleeved

The fiber is stripped and cleaved initially, but without any connector attached. The tubing is cut to size according to the manual to fit the length of the bare fiber piece. The fiber is then inserted into the tubing and guided through it using the inlay nylon pullstring. The basic procedure for preparing the fiber ends is the same as for the temporary connectors. The coating is stripped by a certain length according to the manual, so it fits into the length of the tubing and connectors at the end. As a next step, the strain relief boots and crimp seeve are pushed onto the tubing to make a connection between the connector and the tubing. The epoxy glue is prepared and filled into a syringe with a thin flat needle attached. This needle is inserted into the back of the connector to inject the epoxy into the connector. The epoxy needs to be injected until a small bead of epoxy appears on the outside face of the connector ferrule. The prepared fiber end is now inserted into the connector until it sits at the end of the stripped fiber part. The connector is secured to the tubing by crimping them together, and then the strain relief boot is also pushed and glued onto the back of the connector. The epoxy cures in a few hours and is left overnight to cure. As a next step, the fiber piece that sticks out of the connectors should be cleaved right above the glue bead. This is done with the previously mentioned ruby scribe pen, as any other cleaver does not get close enough to the connector tip. This must be done with precision, as the cleave should not produce any flaking of the fiber tip. If the fiber breaks below the glue bead, one might need to start over, cut off the fiber, and scrap the fiber connector.

The next step is the precise polishing of the fiber from the ground up. The still protruding fiber is sanded down with a 30μm sanding paper until it is flush with the ceramic ferrule. Now, the fiber is inserted into a polishing disc and polished in small steps with flat polishing sheets on a glass plate. The grit size of the polishing sheets gets smaller with every step, starting at 30μm, continuing with 6μm, 3μm, 1μm and finalizing with 0.01μm for the final polish. Each step also involves a visual inspection of the fiber facet with a fiber microscope to determine the current state of the polishing and any defects that might occur. A perfectly clean working environment is a must, as any cross-contamination from the larger to smaller grit polishing sheets can lead to a scratched fiber facet, which can set back the polishing progress to the beginning depending on the damage. So in between every grit size change, the plate, the polishing disk, the fiber, and the polishing sheet are cleaned by clean dust-free air and optical grade isopropanol. The goal is to end up with a connector surface that is free of epoxy, a fiber that is flush with the connector surface, with no defects like digs, chips or cracks on the fiber surface and that the core of the fiber is completely scratch free. Only minuscule and light scratches on the cladding are acceptable if they are not in the region around the core. The goal however should be a scratch free surface after the finishing polish.

This procedure is done on both sides of the fiber. If done right, the finished fiber is a commercial grade fully usable fiber optic patch cable as shown in figure 5.5. Figure 5.4 shows the result of the

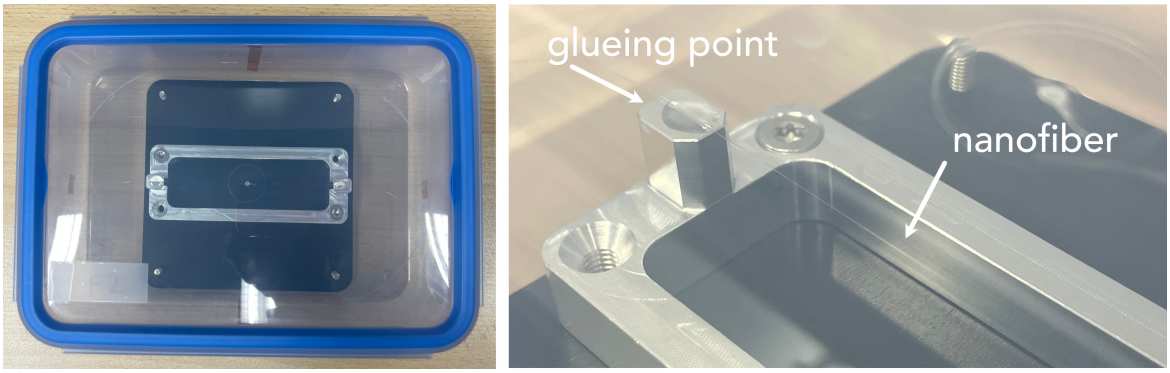

Figure 5.6: The left picture shows a top down view onto the fiber transportation box with a nanofiber installed onto its holder. The right picture shows a close up view of the nanofiber holder with a nanofiber glued on.

polished fiber endface under the fiber microscope. The core is only barely visible and the surface is scratch free.

In total, four patch cables were made aswell as two fibers with only one side being connectorized. The four full patch cables are made from the first batch of Coherent 405HP Ge-core doped fibers. The single sided connectorized fibers were made from a different fiber material that will be discussed in section 6.2. From the four Ge-core doped fiber patch cables two were fabricated without and two with the protective tubing. One of each features a FC-PC (physical contact, flat surface) connector on both sides while the other one features a FC-APC (physical contact, angled surface) connector. The two patch cables without the tubing were tested for their output intensity stability and their coupling efficiency in the same optical setup the bare fibers with the temporary fiber holders

The achievable coupling efficiency does not improve with the permanently connectorized fiber. It reached the same level as the fiber with a temporary fiber connector with respect to the uncertainty of the coupling efficiency. The intensity fluctuations after the fiber also did not show any improvement for the permanently terminated fiber.

5.3 Nanofiber testing

Following the preliminary characterization of the fiber material, the nanofibers pulled by the Berlin group are characterized and evaluated for their transmission and polarization stability. The procedures for managing the nanofibers both within and outside the vacuum chamber are systematically evaluated and mastered. The first initial nanofiber is evaluated under standard atmospheric conditions within its transport enclosure, absent a vacuum environment. Such a tranport enclosure is shown in figure 5.6.

In contrast to the first, the subsequent second and third nanofibers are evaluated under vacuum conditions within the test vacuum chamber. All nanofibers were fabricated from the Ge core doped Coherent 405HP fiber. Notably, the second and third nanofibers were fabricated from a different production batch compared to the first, which should solely differ in the selective cutoff wavelength of the fiber. The three different nanofibers are fabricated using similar pulling profiles, distinguished

solely by their resulting waist diameters. Specifically, the first nanofiber has a waist diameter of $d = 100\,\text{nm} \pm 5\,\text{nm}$, while the second and third nanofibers are characterized by a waist diameter of $d = 200\,\text{nm} \pm 10\,\text{nm}$. All nanofibers exhibit an identical waist length of $2.0\,\text{mm} \pm 0.1\,\text{mm}$ and a taper angle of 2 mrad.

5.3.1 First nanofiber d=100 nm

The first nanofiber was also the first nanofiber prepared to be studied in the setup introduced in chapter 4. The nanofiber is prepared to enable the coupling of light into the nanofiber while preventing its exposure to dust, thereby also enabling an assessment of its condition following transportation from Berlin to Bonn.

Nanofiber preparation

All clean air systems are turned on and checked in advance. The entire workplace is cleaned with isopropanol to remove any residual dust that may have accumulated. The nanofiber transportation box with the first d=100 nm nanofiber inside is placed inside the clean air box together with a new lid that is prepared in advance with two drilled holes opposite each other. The lid was cleaned with soap, afterwards with lint-free wipes and isopropanol, and packaged in aluminum foil.

All procedures are conducted with clean gloves to maintain the cleanliness of the setup. This also ensures the higher standard needed for handling subsequent nanofibers under vacuum conditions, for which any contamination by oil or other residues needs to be avoided. After positioning the transport box in the middle of the working area inside the clean air box, the lid is carefully opened and placed upright. In this way, one ensures that no dust can be churned up, as could be the case if it were laid flat. To provide safe transport, the entire fiber is spooled up before and after the nanofiber holder and fixed with kapton tape inside the transport box. This tape needs to be removed by hand or with tweezers without working above the nanofiber region to reduce the risk of dust contamination.

Due to the exposure of glass resulting from the partial stripping process, the fiber exhibits increased susceptibility to strain, particularly when subjected to sharp edges such as those presented by the glue interface. This is why unspooling of the fiber needs to be done with caution to avoid allowing the fiber tail to drop onto the nanofiber region by mistake or putting strain on the gluing point of the fiber to the holder. Because if the fiber breaks at that point, splicing the fiber back together becomes impossible, and the nanofiber has to be scrapped. The unspooled fiber is threaded through the holes in the prepared lid. Subsequently, the section of the fiber located within the box, right after the gluing points, is again affixed to the box to function as a strain relief. The lid is put on the box and closed. The fiber tails coming out of the lid are affixed with kapton tape as a second strain relief point and to protect the fiber from dust from the outside by closing the holes.

Transmission test

As the next step, the transmission of the nanofiber should be tested under normal atmospheric but dust-free conditions. Therefore, a small self-built mounting bracket for the nanofiber box is attached to the optical table on a second level above the other optics to be able to observe the nanofiber region

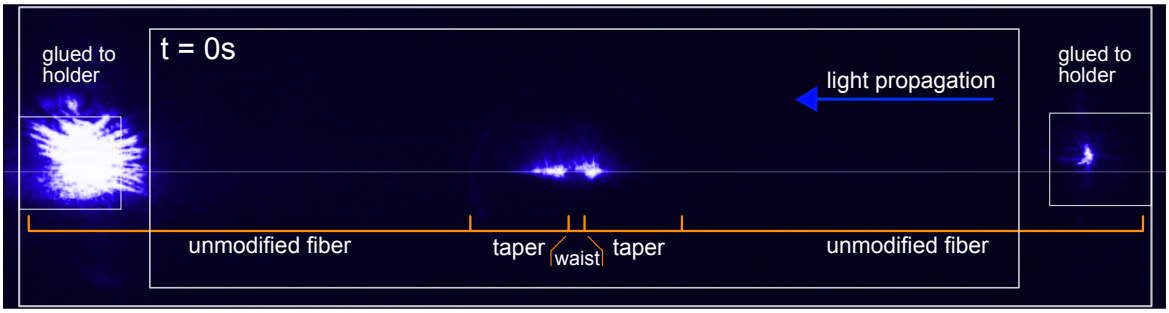

Figure 5.8: First nanofiber viewed from above onto its nanofiber holder. 399nm is coupled into the fiber resulting in scattering in the taper region, showing the fiber at $t = 0\,\mathrm{s}$ of light exposure. A bright spot on the left glueing point is the result from light scattering from the right taper onto the metal and shining into the camera.

while light is coupled into it. Figure 5.7 shows the nanofiber in its transportation box mounted on the table. The Imaging Source monochrome DFK 72AUC02 CCD camera with a 6-60mm focal length F1.6 aperture c mount lens is mounted above the optical table right below the flow box to capture the nanofiber continuously in its transportation box.

The highest achievable coupling efficiency of the setup for the Coherent 405HP fiber was tested before. With an aspheric Thorlabs $f = 9.6\,\mathrm{mm}$ C060TMD-A lens, an output of $f = (440 \pm 9)\,\mu\mathrm{W}$ was reached for an input power level of $f = (1\,500 \pm 3)\,\mu\mathrm{W}$ in front of the fiber coupler for a 1 m normal Coherent 405HP fiber piece. This results in a 29.3% coupling efficiency, which should be reached every time if the coupling is fully optimized. The test data from the Berlin group shows that because of the fabrication of a nanofiber with a $d = 100\,\mathrm{nm}$ waist, its relative transmittance compared to the unpulled fiber was reduced to 45% 399 nm. The transmission reduction due to the nanoregion can be deduced, by assuming that the theoretically achievable coupling efficiency of this nanofiber is the same as that of the unpulled fiber, because they are made from the same fiber material. A favorable outcome would be for the observed reduction in transmission to match the data provided by Berlin, as this would indicate that no significant damage or dust contamination occurred during the preparation of the nanofiber or throughout the shipping process.

Figure 5.7: Nanofiber in transportation box on the fiber testing table after the lid was swapped and the fiber prepared.

For the following tests, the nanofiber ends are terminated with a temporary bare fiber connector. The nanofibers coupling is optimized, reaching 210 µW of power at the output. Assuming that the same coupling efficiency as in previous tests was reached, 440 µW of light are coupled into the fiber right before the nanoregion. Now one can deduce that the loss due to the nanoregion is $(230 \pm 3)\,\mu\mathrm{W}$ which then leads to a relative transmission of 47.7% for the whole fiber. This result matches the measured 45% quite well if one considers all measurement uncertainties and the fact that the nanofiber was fabricated from a different batch of fiber material.

Observing the nanoregion of the fiber with the camera, as can be seen in figure 5.8, shows that the

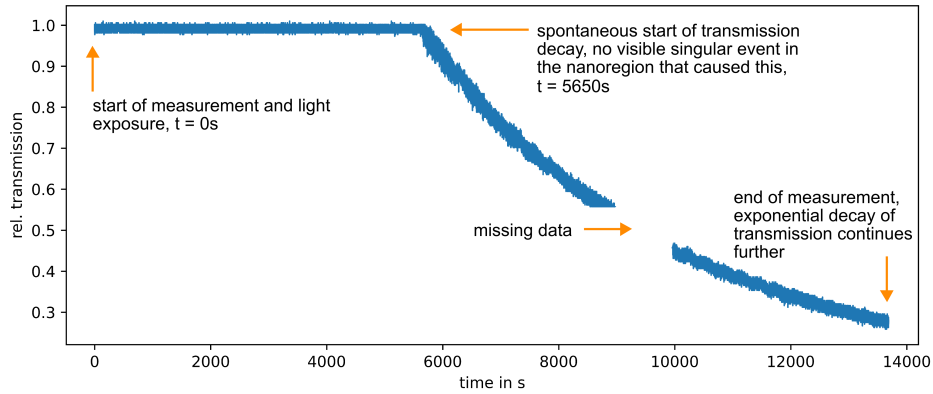

Figure 5.9: Relative transmission of the first nanofiber over time. Showing a sudden drop in transmission with an exponential like decay.

fiber is intact and scatters some light at the right and left gluing points and from both taper regions. At the left gluing point it also appears to be a lot of scattering, but this is not light scattering from the fiber. It is mostly light that is lost in the first taper region, shining onto the metal holder on the left and overexposing the image. The scattering near the right glueing point can be explained by a backreflection of the light from the left part of the nanofiber holder. These observations are consistent with the observations from the Berlin group. This loss in the taper region was observed by the Berlin group, too, while the nanofiber was fabricated. The nanofiber and holder have been added to the picture afterwards, as the camera cannot capture them appropriately due to its exposure time. The view direction is directly from above onto the fiber holder. The taper and waist region are free from any singular dot-like scatterers, which would indicate dust particles and a further reduction in transmission. This indicates that the fiber did not suffer any measurable or visible damage from transit to Bonn, and the process of the fiber preparation and lid exchange did not introduce any dust onto the nanoregion of the fiber. After optimizing the fiber coupling at lower power levels before, the nanofiber is now again exposed to 1.5 mW of 399 nm light for a longer period of time while its transmission of initially (210 ± 3) µW and scattering in the nanoregion are monitored. The relative transmission over time can be seen in figure 5.9. The transmission remains stable for the initial 5650 seconds of light exposure, after which it begins to decrease similar to an exponential process. This decline persists for the remaining observation period of 8050 seconds, ultimately reaching 30% of the initial transmission after a total duration of 13700 seconds of constant light exposure. After which the measurement is stopped due to storage limitations of the oscilloscope used. The general trend of an exponential decline continues and reaches 0.1 µW in transmission after roughly 20 hours of constant 1.5 mW light exposure. This equals 0.05% of the initial transmission. The transmission does not recover after blocking the beam for several hours and unblocking it again. Observation of the captured images of the nanoregion of the nanofiber shows that there is an evolution from the start $t = 0$s in figure 5.8 towards the start of the exponential decrease, but no single event such as a dust particle that settles on the fiber could be made out by a single bright dot scattering light. There is a continuous transition from both taper regions lighting up equally over to the right one, getting brighter, while the left one gets darker over time. The visual transition starts to set in approximately 1000 seconds after the start of light exposure and progresses without interruption to the end of the measurement. The transition speed can be described by a slow change, that gets faster, stagnates, and gradually slows

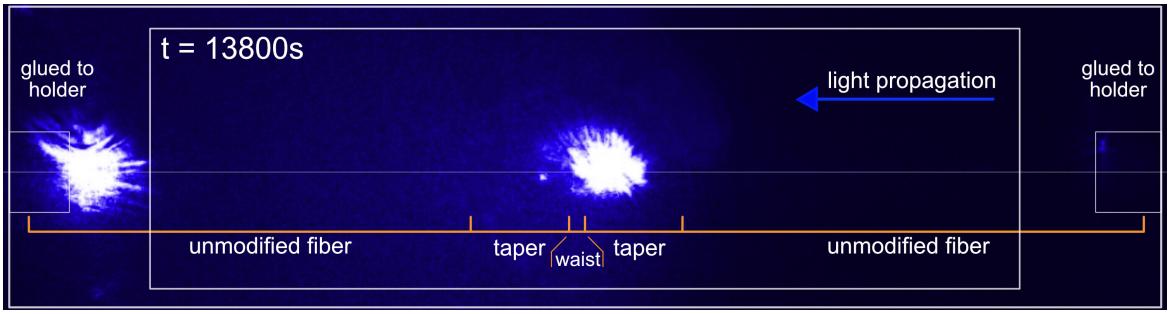

Figure 5.10: First nanofiber viewed from above onto its nanofiber holder. 399nm is coupled into the fiber resulting in scattering in the taper region, showing the fiber at $t = 13\,800$ s of light exposure. A bright spot on the left glueing point is the result from light scattering from the right taper onto the metal and shining into the camera.

down again. Figure 5.10 shows the end of the transition at $t = 13\,800$ s. Quantitative analysis of this phenomenon was not feasible due to highlight clipping, which was a consequence of the camera's limited dynamic range. These observations lead to the question of whether this decline in transmission for 399 nm light over time also occurs for a nanofiber in vacuum instead.

5.3.2 Second nanofiber d=200 nm

The second nanofiber is placed in the test vacuum chamber and is tested for transmission and polarization stability under vacuum conditions. It has a waist diameter of $d = 200$ nm instead of $d = 100$ nm like the previous one, because for the Berlin group this set of parameters is easier to fabricate for higher transmission values is easier to fabricate with a higher transmission.

Nanofiber preparation

The initial preparation of the nanofiber is based on the basic procedures of the first nanofiber, but now expanded to be vacuum compatible. The installation is carried out again under dust-free conditions inside the clean air box with special care to not bring in any dust from the outside. In addition, the working area inside the clean air box is completely covered with two sheets of aluminum foil for vacuum applications. All procedures are carried out with two pairs of clean gloves worn over each other to protect all parts touched from any contamination by oil or other residues, even if one glove layer breaks. In case the gloves break, they will be replaced by new ones. All tools required for assembly that are not introduced into the chamber and the nanofiber transport box are meticulously cleaned with isopropanol and subsequently arranged in the working area. New gaskets and screws and nuts that were cleaned for vacuum use for the nanofiber holder are also placed within the working area. The flange reaching into the clean air box is also meticulously cleaned with isopropanol before its screws are removed. Particular care is very important to prevent damage to any parts, especially the knife edge of the flange. Upon removal of all outer screws, the flange is carefully removed from the chamber, ensuring that the gasket does not fall onto the nanofiber holder mounted on the inside of the flange. The optimal method involves slightly tilting the flange upward during removal while taking care not to incline it excessively so that the nanofiber holder could make contact with the chamber

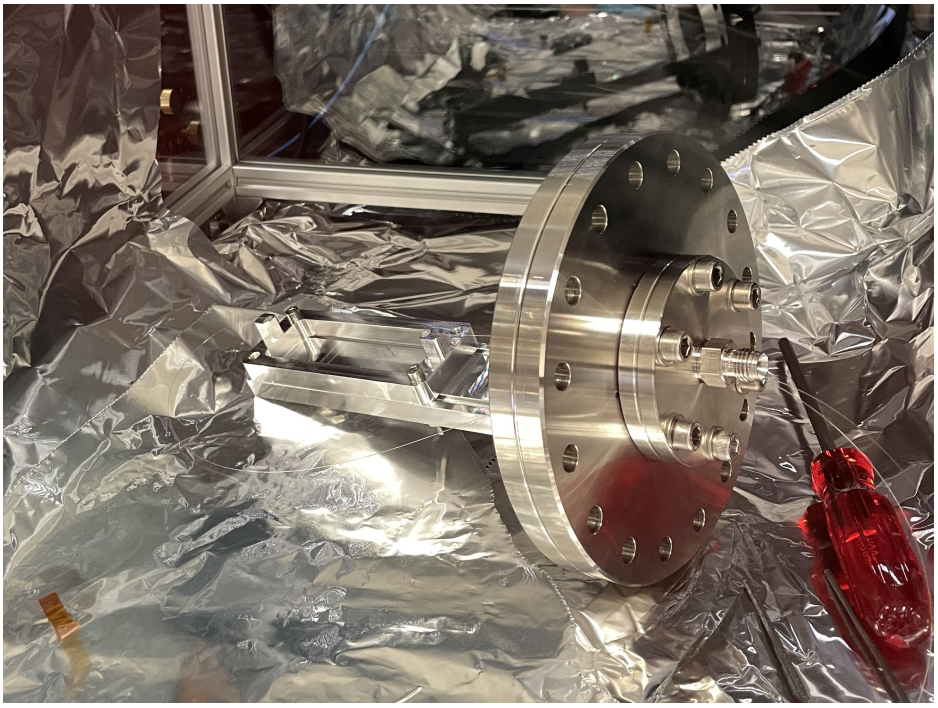

Figure 5.11: The second nanofiber is attached to the inner side of the vacuum chamber flange onto the nanofiber adapter. Both fiber ends are going into the vacuum fiber feedthrough.

interior. After removal, the flange is put aside and the open vacuum chamber is covered with a sheet of aluminum foil. Before continuing with the nanofiber installation, the old teflon fiber feedthrough seal needs to be removed. Consequently, the Swagelok screw is loosened and any previously installed fiber is extracted. The seal is subsequently expelled from the interior with a bit greater force using a cleaned long hex screwdriver, because of the tight fit within the opening when it was closed for vacuum usage before. Then, the nanofiber is prepared. The transportation box with the nanofiber inside is placed in the middle of the working area and its lid is carefully opened and put aside. Subsequently, the kapton tape and screws that fixate the nanofiber holder in the box are removed. Because this work is again done close to the nanofiber region, a high level of attention is needed on every step, especially with taking out the screws. The nanofiber holder with the glued nanofiber is then taken out of its box and moved over to the flange with its adapter for the nanofiber holder. It is attached to the adapter plate by screws that were cleaned for vacuum use. Additionally, both fiber ends are passed through the open fiber feedthrough port on the flange and subsequently through a new telfon seal, each having an individual aperture. The fiber end pointing towards the flange can be pulled through without much concern, whereas the fiber end on the other side of the holder, pointing away from the flange needs to be guided more carefully, as a bending of the fiber directly after the glueing point, where it is beside the waist region the most fragile is needed. The bending radius is adjusted by taking or giving the fiber a bit more slack by pulling it through the feedthrough. For the main experiment, an updated design for the fiber holder will be used that features fiber guide grooves underneath to fix the fiber, which reduces the strain that is placed onto the fiber at the glueing point. A new gasket is used for the flange and ideally is held on to the flange with retaining clips for easier installation without having to

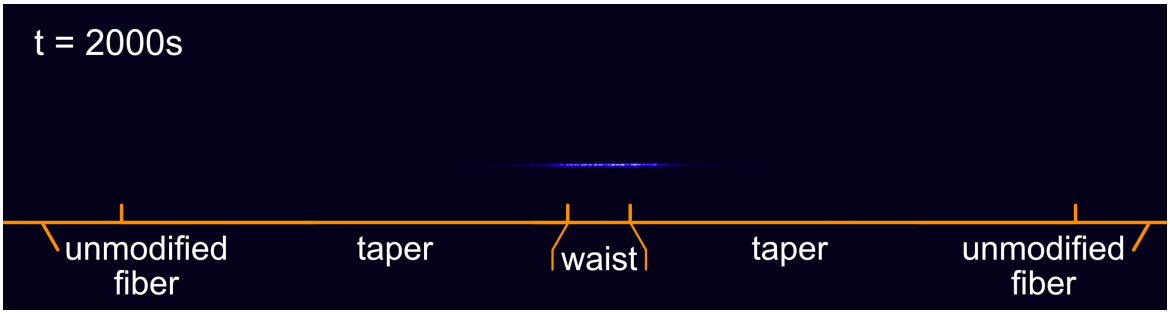

Figure 5.12: Second Nanofiber inside the vacuum chamber with 399 nm light coupled into it, scattering most of the light in the waist region.

worry about a falling gasket that might hit the nanofiber holder and break the fiber. After another careful inspection of the nanofiber for damage or dust, the flange with the installed nanofiber is again attatched to the vacuum chamber.

Afterwards, the swagelok screw is closed such that it presses the Teflon cone into the fitting which seals the fiber feedthrough. Subsequently, the chamber is evacuated according to the protocol described in section 4.3.1 and afterwards checked for leaks as described in section **??**. If the leak test returns a positive result and the vacuum pressure stabilizes in the lower e-07 hPa to high e-06 hPa regime, the fiber ends are prepared with the temporary fiber terminators and for the first time after the nanofiber fabrication light is coupled into the nanofiber. A quick check with a fiber testing pen shows that the fiber indeed transmits light and no fatal damage in the preparation, assembly and evacuation procedure occured.

Transmission test

This second nanofiber is tested for its transmission behavior under vacuum conditions, after the first nanofiber showed a strong exponential decay in transmission in a few hours under ambient pressure conditions. Like in section 5.3.1 the transmittance of the nanofiber for 399nm light using the data from Berlin is checked, by assuming that the same coupling efficiency as for an unpulled bare fiber could be reached. The nanofiber reaches $(300 \pm 3)\,\mu W$ in transmission at an input power of $(1\,180 \pm 9)\,\mu W$. For an optimal coupling where 350uW for an unpulled fiber would be expected, a transmittance of $(85.1 \pm 0.8)\,\%$ can be calculated for the nanofiber. This matches the data for 399 nm from Berlin with 85% accurately. After slight readjustments of the coupling, the transmission of the nanofiber suddenly dropped by 46.6% to $(160 \pm 3)\,\mu W$ in transmission and could not be recovered from that by re-optimizing the coupling. The data capture was not running yet, so there is no data on this sudden drop available. Subsequently, the capture of the data is started, and the camera observes the nanofiber in the chamber as described in Section 4.5.

In contrast to the d=100 nm nanofiber, mainly the waist region and only parts of the taper region scatter light. There is no clear loss peak in the taper as before. This might be the result of a smoother transition for the d=200nm nanofiber as the overall measured transmission loss is much lower in comparison. The unmodified fiber parts also show some scattering that was not visible for the $d = 100$ nm nanofiber, due to the shorter exposure time of the camera and the much higher scattering loss in the taper region

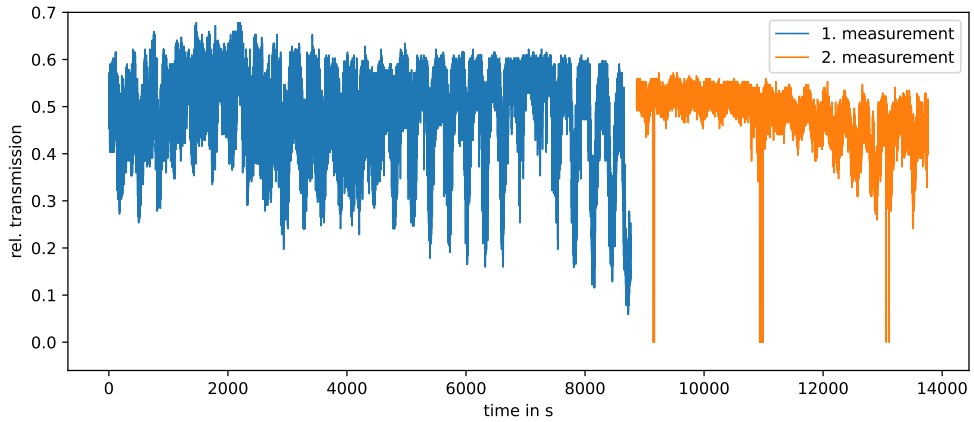

Figure 5.13: Relative transmission of the second nanofiber over time. The measurement is broken up in two parts.

which quickly overexposes the camera. However, this glow in the unmodified fiber region is visible to the naked eye for both nanofibers, but is more prominent for the $d = 200\,\text{nm}$ source compared to the scattering in the waist and taper region. Figure 5.12 shows the nanofiber in the chamber with the exposure level adjusted to see the scattering in the waist region.

The transmission measurement is separated into three measurement runs, as it turns out that the observation time needs to be longer than the oscilloscope can record in one go to see a significant change this time. So after the second measurement, the oscilloscope is exchanged for the Picolog mentioned before in Section 4.5, which can record almost indefinitely at a sampling rate of one sample per second, which is sufficient for long-term measurements. In figure 5.13 the first two measurement runs can be seen. They are separated in time by two days, but in between the laser light is blocked, so the exposure time to 399 nm light corresponds to the time on the y-axis. The transmission is normalized, corrected for input power fluctuations, and adjusted to the transmission drop that occurred before but was not recorded. The time evolution of the transmission of the nanofiber evolves in a manner completely different from that of the first nanofiber. It shows fluctuations characterized by a gradual cyclic nature, with an amplitude that reaches up to 60% of the full range. There is a slight downward trend over the full 8760 seconds of light exposure. The subsequent second measurement two days later shows again a similar cyclic pattern where the amplitude grows over time. The evolution of the cyclic pattern is not interrupted by the four times the laser light in front of the fiber was blocked on purpose, where the relative amplitude goes to zero. The downward trend of the first measurement continues for the next 7500 seconds of light exposure.

The subsequent third measurement is conducted for 82 hours, which is a much longer time period than the first two measurements to gain more data on the time evolution of the nanofiber and to validate if a sudden change in transmission behavior does occur, such as for the first nanofiber. The result of the measurement can be seen in figure 5.14. Again, the transmission is normalized and corrected for input power fluctuations, so it matches the relative transmission of the first and second measurements to make it a consecutive time series. Here, one can see a clear continuation of the downward trend from 0.426 to 0.256 relative transmission over the full 82 hours. A clear exponential decay like before for

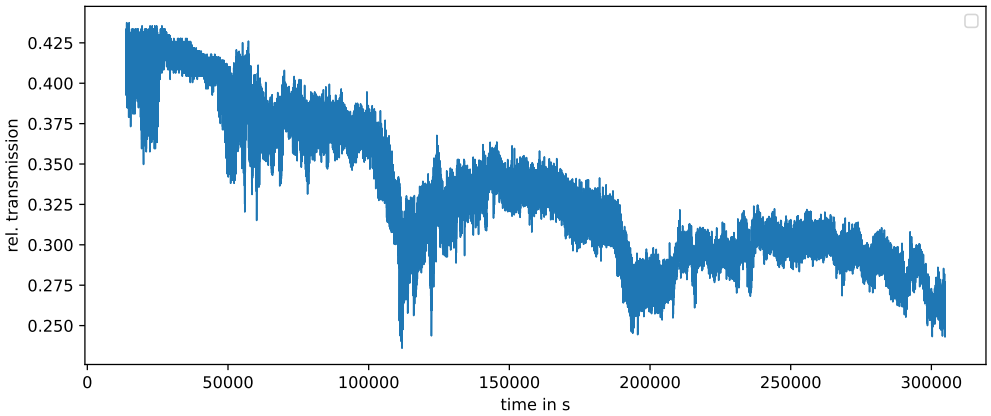

Figure 5.14: Relative transmission of the second nanofiber over time.

the first nanofiber can not be attributed. The transmission increases and decreases over hours without showing a clear pattern other than the constant downward trend. In contrast to the first nanofiber, the nanofiber region does not show a onesided change in the intensity of light scattered. The intensity in the nanoregion as a whole changes in correspondence to the measured transmission. At the end of the measurement the waist region can only be seen by increasing the exposure in postprocessing.

In order to exclude a drifted coupling as the source of the observed transmission reduction, the fiber is cut 15 cm after the incoupler, and the output power after this fiber piece is measured. The measured power after this so called cutback is 0.433mW in contrast to 0.105 mW at the fiber output after the nanoregion before the cutback. It turns out that the coupling efficiency at a power in front of the fiber of 1.480 mW is with 29.2% almost the same as it was estimated at the beginning. However, this also confirms the initial deduction of the reduced transmission due to the nanofiber region of 85%, because the assumption that optimal coupling for the nanofiber corresponds to the same level of coupling efficiency observed for an unpulled fiber holds true. This means that in the cutoff fiber part, which also includes the nanoregion in the vacuum chamber, a transmission reduction of overall 75.8% relative to the power coming from the fiber part, while still coupling in 399nm light, has developed. This whole process evolved in around 86 hours of 0.433mW of 399nm light being coupled into the nanofiber due to a still unknown degradation process. In consequence the next tests will be another nanofiber transmission test under vacuum conditions, as well as general fiber material tests, to explore what influence the nanofiber region has on this observed degradation process.

5.3.3 Third nanofiber d=200 nm

To rule out production-related problems with the first batch of nanofibers being the source of light-induced transmission degradation, a second $d = 200$ nm nanofiber from a new production run is tested again under close to UHV conditions for transmission stability.

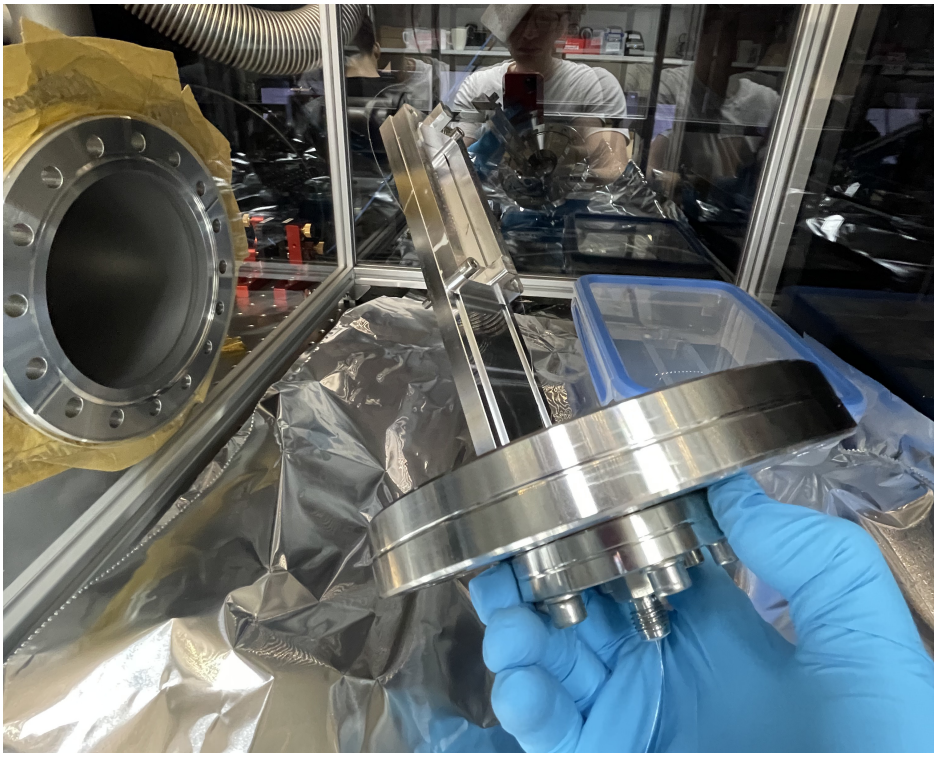

Figure 5.15: The third nanofiber is attached to the inner side of the vacuum chamber flange onto the nanofiber adapter. Both fiber ends are going into the vacuum fiber feedthrough. The opened vacuum chamber is depicted on the left.

Nanofiber preparation

The nanofiber preparation and installation procedure is mainly the same as that of the second nanofiber in Section 5.3.2. Following the steps from the first nanofiber vacuum assembly and remembering the learnings made, makes it much less prone for errors to occur, and the installation is done much faster and makes handling easier. The third nanofiber is successfully transferred from its transport box to the vacuum chamber flange adapter without visible damage, as can be seen in Figure 5.15. The segment of the fiber extending away from the flange is again directed downward and guided beneath the holder to the fiber feedthrough. This arrangement prevents problems during the chamber assembly and mitigates the risk of the fiber section falling onto the nanofiber region, which might lead to damage. The flange is inserted into the vacuum chamber by again also exchanging the flange gasket and the teflon fiber feed-through cone for new ones. Evacuating the chamber with the known procedure leads to the pressure stabilizing at 7.5×10^{-7} hPa after closing the valves. The fiber ends are then prepared with temporary fiber terminators. A quick check with a fiber testing pen shows that the fiber indeed transmits light and no fatal damage occurred in the preparation, assembly, and evacuation procedure.

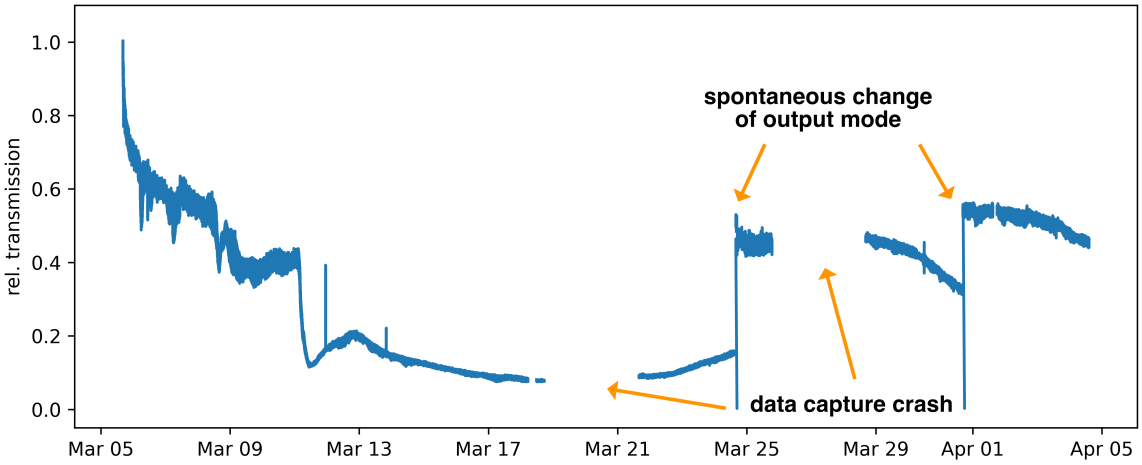

Figure 5.16: Relative transmission of the third nanofiber over time in days of the month. One month is captured in total.

Transmission test

The measurement of the transmission over time begins with the evaluation of the coupling efficiency and transmission losses that result from the nanofiber fabrication. The power level in front of the fiber is reduced to (460 ± 5) µW to be closer to the power levels needed inside the fiber for the main experiment, which will probably be in the 10-200 µW range. With an optimal coupling the power after the nanofiber is (113 ± 3) µW. With an assumed coupling efficiency of (29.3 ± 0.3) % this corresponds to a transmittance of (83.8 ± 0.5) %, due to the nanofiber region. This does not match the data for this third nanofiber from Berlin very well, as they measured a transmittance of about 90% at 399 nm after pulling the fiber. However, this can be explained by a not purely Gaussian beam shape with quite a few abberations. This can be observed when the beam on the fiber testing table is captured by a beam profiling camera. These abberations evolved between the second and third nanofiber tests and could be pinpointed by process of elimination to the 10 m fiber that supplies the fiber testing table with 399 nm light. The fiber facet shows a ring around the core, which is not usual. Due to the lack of a replacement fiber and the beam still being Gaussian just with added abberations, it is used anyways. The beam quality might lead to a poorer than expected coupling efficiency. The deviation of the transmittance of the nanofiber from the data from the Berlin group therefore, does not mean that the fiber was damaged or got polluted with dust. Figure 5.16 shows the normalized transmission corrected for input fluctuations of the third nanofiber under vacuum conditions. The transmission evolves similar to that of the second nanofiber, but without the oscillations in the first few hours. An exponential decay in transmission is immediately observable from the beginning. After about 5 days of continuous exposure, the transmission reached a level of 40% of the initial transmission and starts to drop even faster to a much lower level of transmission of around 10% rising again slightly over the span of two days and continues to drop even lower. What is even more suprising is the sudden jump in transmission on 25th of March to 50%. The output mode changed. The mode before and after this event is shown in figure 5.17. The mode before March 25 looks somewhat like a LP_{02} mode while after the change it shows again a basic LP_{01} mode. This behavior repeated itself before April 1. The input coupling was not changed at all times. Only the output was adjusted when the change occured.

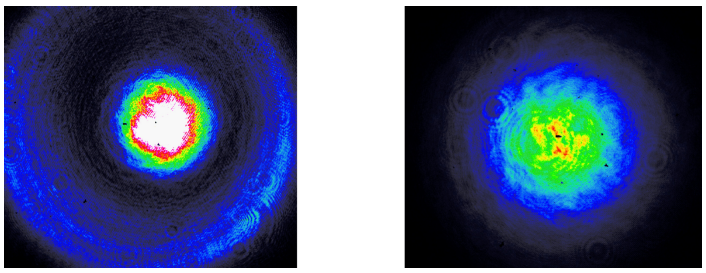

Figure 5.17: Nanofiber output before March 25 on the left, output on March 25 and afterwards on the right.

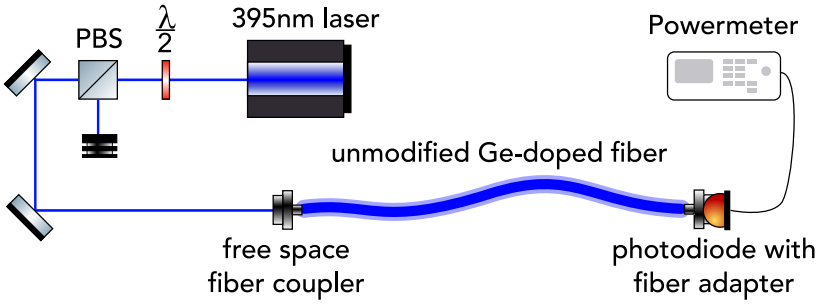

Figure 5.18: Basic fiber testing setup for testing unmodified Ge-doped fibers at high 395nm transmission levels. A photodiode measures the output after the fiber.

After one month of constant exposure the measurement was stopped. The fiber shows a transmission of $(32.9 \pm 0.2)\,\mu W$, after doing a cutback of the whole nanofiber region leaving only 20 cm the output changes to $(76.2 \pm 0.1)\,\mu W$. A whole $(52.4 \pm 0.2)\,\%$ of transmission is lost in the cutoff part.

5.4 Fiber material tests

All the tested nanofibers show an unexpected degradation behavior in the transmission of coupled 399 nm light over time. This occurs at low power levels of only a few hundred μW of light. To determine whether the nanofibers or the fiber material itself contribute to this degradation, the unmodified Coherent Ge-doped fiber material is subjected to a series of transmission tests.

Numerous fiber pieces were examined for their transmission behavior at 399 nm and 395 nm light. Because the observed degradation behavior often differed in type and severity, a systematic analysis proved to be very difficult and lengthy. This chapter therefore gives an overview of the observations made. An attempt to explain some of these observations can be found in Section 5.5.

5.4.1 power dependence

We approximate an increase in intensity within the core in the taper region of the $d = 100$ nm nanofiber by a factor of the order of 100 compared to an unmodified fiber. By taking only the decreasing fiber dimensions into account, this easily overestimates the intensity increase that happens due to the

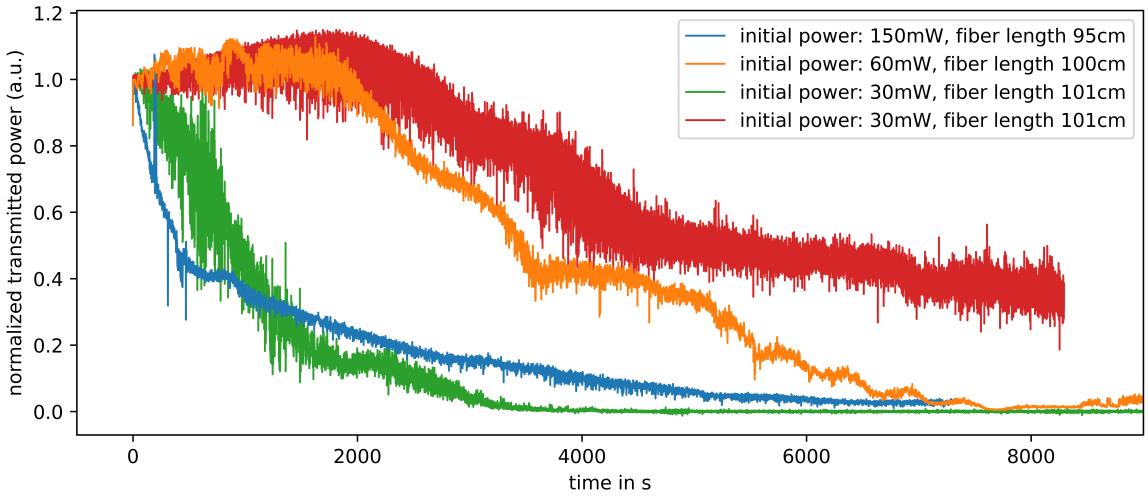

Figure 5.19: Normalized transmitted power over time of four fibers tested at different power levels at 395 nm

tapering, due to the changing guiding properties of the fiber along the taper. However, it gives an approximate power level to test the unmodified fibers at. The idea is to reach peak intensities in the Ge-doped core of the unmodified fibers similar to those that occur in the nanofibers to compare their transmission behavior. The unmodified Coherent Ge-doped fibers are tested in a different setup to be able to work with 399 nm/395 nm light at a higher power level than possible on the fiber testing table. In its essence, the two separate setups consist of a laser source of 399 nm and 395 nm, a $\lambda/2$-plate in front of a polarizing beam splitter for easy power adjustment, and a basic beam coupling setup consisting of two mirrors and a Thorlabs free space fiber coupler as illustrated in figure 5.18. For these tests, each piece of fiber has a length of one meter. The fiber ends are prepared with temporary fiber holders. The output power after the fibers is recorded with a Thorlabs PM100D with a S121C photodiode power sensor with an attached fiber adapter. Light is coupled into the to be tested fiber piece, and the coupling is optimized to the maximum. The power after the fiber is adjusted by turning and setting the $\lambda/2$-plate. The separate power levels tested in these first runs are 30 mW, 60 mW, and 120 mW. They are measured after the fiber. A fiber is subjected to one certain amount of power for the whole measurement, and the transmission is captured over time. After one measurement at one power level, the fiber is exchanged for another one, and the entire coupling and testing procedure is repeated. A selection of the transmission behavior observed at 395 nm over time is shown in Figure 5.19. These graphs summarize the most important features of the observations made in these test runs. It shows that the unmodified fiber is subjected to a decay in transmission over time with big fluctuations in shape and severity. A drifted coupling over time is excluded by trying to re-optimize the coupling to regain the transmission. However, this did not make any difference. At these power levels, all fiber pieces tested lose their transmission by at least 99% compared to the initial power levels after a couple of hours. No systematic correlation could be found between the initial power level and the time it takes for the transmission to decay to a certain level. As Figure 5.19 shows, the time for the transmission to decay to 40%, chosen as an arbitrary level, is on the same order of magnitude, but can differ for a different fiber piece at the exact same power level by a large margin. Furthermore, the shape of the decay is not the same for repeated measurements. In some cases, the

transmission is stable for multiple minutes, before it starts to decay, as shown in Figure 5.19 for the red and orange graphs. Overall, the transmission also fluctuates by up to 10% on the second timescale, which is not the result of laser power fluctuations which were verified in a separate measurement by also monitoring the power in front of the fiber with a pick-off plate and a separate photodiode.

By gradually increasing the input power (the power measured in front of the fiber) after the transmission of a fiber reached one percent of its initial transmission, the output power of most fibers (the power measured after the fiber) did not rise proportionally to the increase in input power but stayed at the same level as before. However, further increasing the input power to a maximum of 500 mW led to a sudden jump in output power for some fibers. Up to 35% of their initial transmission capability was restored. Sweeping of the input power was found to be even more effective in regaining some of the transmission capability. However, turning down the power again led, in most cases, to a jump back down to the state of almost complete loss of transmission as it was before. In the other cases, the output power reduced proportionally to the reduced input power. For those fibers, a transmission decay similar to that seen in Figure 5.19 could be observed again. Because this behavior was only observed for a few of the fibers tested and could not be reproduced on purpose, a more in-depth analysis of this behavior could not be performed. Fibers that regained some of their transmission after such a described input power sweep showed another interesting behavior. When blocking the beam in front of such a fiber and unblocking it again after a few seconds, a delay of several seconds could be observed before the output power rose again. So even though the beam was already unblocked, the fiber did not transmit any light, only after the described delay of a few seconds the transmission did suddenly rise to the same level before blocking the light. This behavior could be repeated multiple times for the same fiber, but after a few minutes, the transmission broke down again and another sweep of the input power could not bring it back.

Another observation on these fibers with almost complete loss of transmission could be made. When the fibers reached levels of about > 90% transmission loss, the fiber output begins to flicker on the second timescale in a random pattern. This means in this case that the output power after the fiber jumps within a certain range fast up and down with some smooth transitions in between. Figure 5.20 shows an example of flickering of a one-meter fiber that degraded to below 1% of its initial transmission of 60 mW. The transmission exhibits a baseline level of several tens of μW, with sporadic peaks that reach 200 μW. If now half of the fiber (50 cm) at the end of the fiber is cut off, and the fiber end that was cut is cleaved and prepared again with a temporary fiber holder, the sporadic peak behavior remains and repeats even more often. On the other hand, about 20% of the initial transmission could also be regained as shown in figure 5.21.

As the fibers exhibited strong transmission degradation at power levels greater than 30 mW in transmission, lower power levels should also be investigated. Figure 5.22 shows the transmission over time of two fiber pieces, each 1 m long. One is tested at 5 mW in transmission at 399 nm and the other one at 5 mW in transmission at 395 nm. This reveals a similar steep transmission loss in the beginning of the measurement in comparison to the higher power transmission tests. Nonetheless, this trend does not persist at the same rate. The degradation happens on a much larger time scale. In about 18 days of constant exposure, the fiber tested at 5 mW in transmission at 399 nm reached a level of about 80% of the initial transmission. It settled on this level after an initial degradation. On 10 April, an adjustment

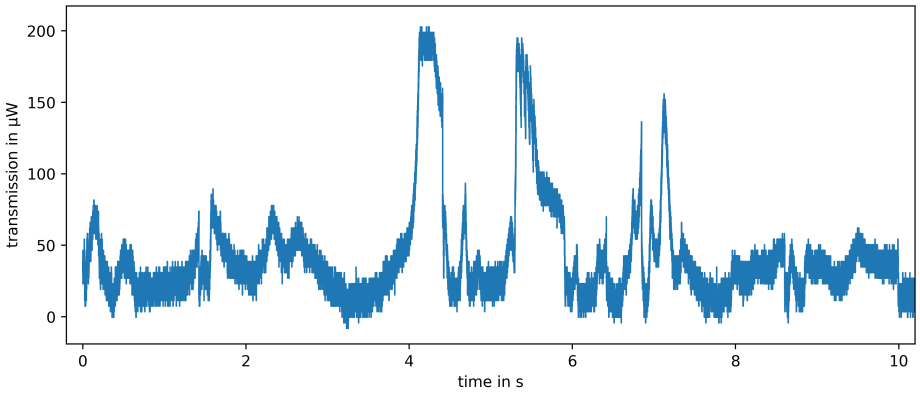

Figure 5.20: Intensity fluctuations over time measured after a fiber. The fiber degraded to a transmission level below 1% relative to its initial transmission of 60 mW.

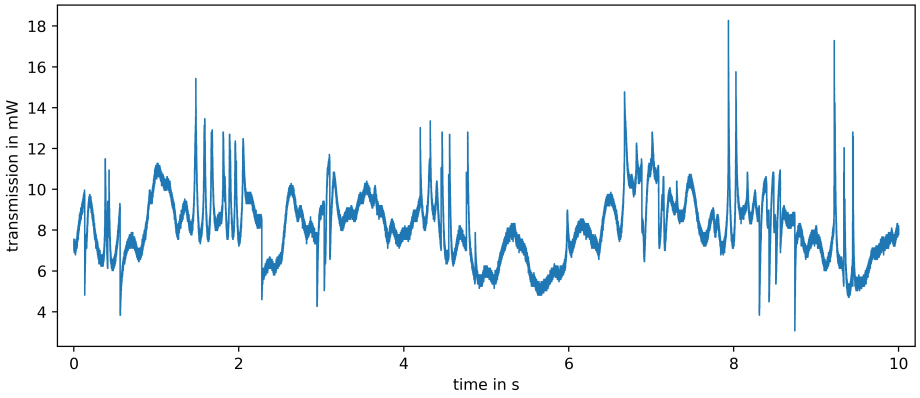

Figure 5.21: Intensity fluctuations over time measured after a fiber. The fiber degraded to a transmission level below 1% relative to its initial transmission of 60 mW. Half of the fiber was cut off.

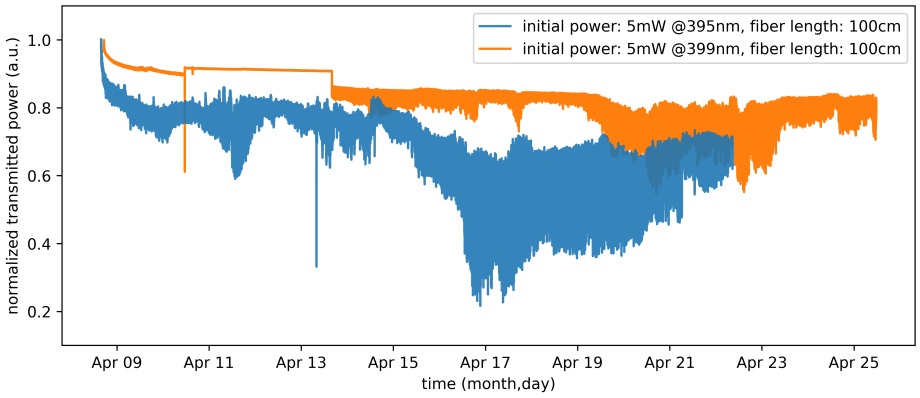

Figure 5.22: Relative fiber transmission over time of two fibers tested both at 5 mW in transmission. Blue is depicting the fiber tested at 395,and orange the fiber tested at 399 nm

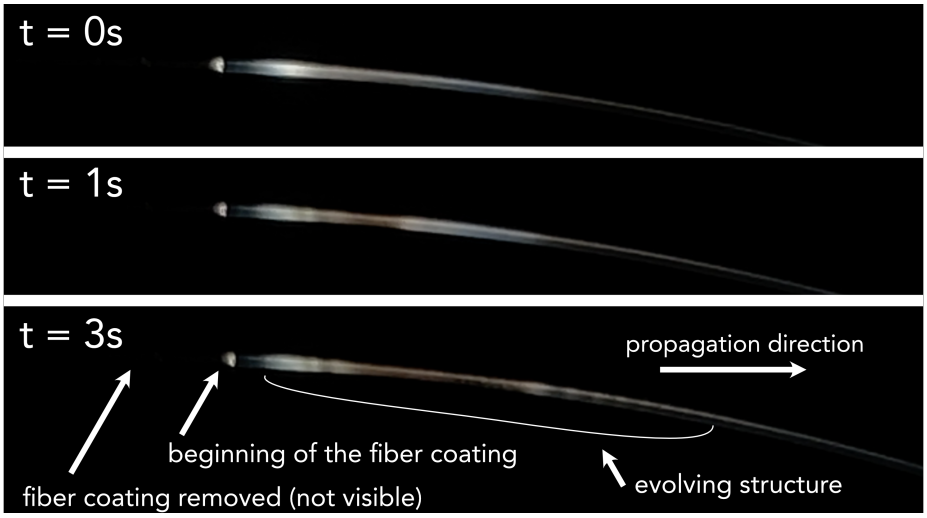

Figure 5.23: A fiber where the coating is removed in the beginning. 395nm light is coupled into it. By blocking and unblocking the coupled beam a grating like structure evolves and expands in the coated fiber part. Reaching its final structure after 3 s

of the fiber coupling led to a slight increase in transmission. However, in the late afternoon of April 13, the transmission showed a sudden drop in transmission and a fluctuation pattern with growing amplitude evolved. Another coupling optimization did not increase the transmission again or reduce transmission fluctuations.
In about 14 days of constant exposure, the fiber tested at 5 mW in transmission at 395 nm reached a level of about 68% of the initial transmission. The initial drop here was much deeper and the transmission fluctuates early on, dipping deeper down to the 25%, before rising again over the next days. Quite a lot of these fluctuation are situated in the mHz regime, judging from a spectral analysis of the time series, and therefore evolve very slowly over time. Their amplitude also evolves over time. Laser power fluctuations for all these observations can be mostly excluded as it was checked regularly and none of the shown fluctuation patterns could be observed in the power in front of the fiber. Due to time constraints no further measurements at these power levels and timescale were conducted.

While observing the fibers that degrade at 60 mW of 395 nm light, another observation could be made. The polymer coating of the fiber needs to be partially removed to use them with temporary fiber holders. In the spot after the fiber holder where the coating was not removed, some fibers showed a sort of grate pattern in the light that is scattered in this part as shown in figure 5.23. If the light is blocked and unblocked again, this pattern evolved on the second time scale. It evolves from a uniform glow of this region ($t = 0$ s) that moves forward in the propagation direction of the light ($t = 1$ s). This bunch of light stretches, and by doing so the grate pattern evolves after about $t = 3$ s. After that, the pattern remains constant. The procedure can be repeated multiple times and the pattern evolves in the same way with the same characteristics. After a couple of minutes to half an hour and the transmission degrading further, the pattern faded and the part where it evolved just showed a uniform glow again. Blocking of the beam does not lead to any evolving structure. Because of its unpredictable appearance after some time in a degradation test, this effect could not be investigated further.

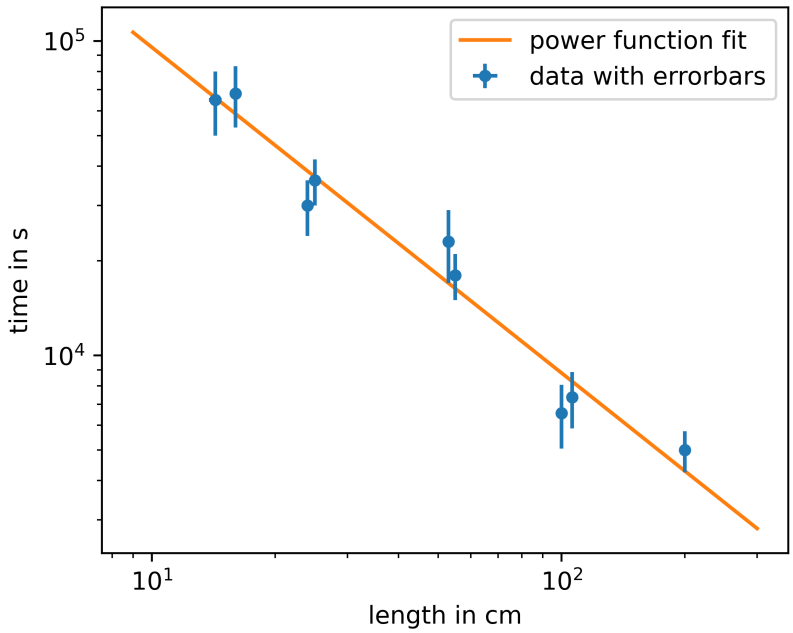

Figure 5.24: Time for a fiber to degrade to 5% of its initial transmission at 395 nm and 60mW in transmission plotted against the length of the fiber piece. A power function is fitted to the datapoints

5.4.2 length dependence

To get a grasp of the fiber transmission degradation process, the length dependence of the fiber on this process was investigated. Fiber pieces of different lengths between 14 and 200 cm were tested for their transmission behavior at a wavelength of 395 nm and 60 mW in transmission. Each of the fibers degraded to the low single digit percentage of the initial transmission with similar shapes in decay as shown in section 5.4.1. An arbitrarily chosen threshold value of 5% of the initial transmission marks the time it took for the fiber to count as degraded. The results of this measurement are shown in figure 5.24. They are plotted on a log-log scale and fitted by a power function, since it showed that, at least for the tested fiber lengths, a length dependence on the degradation time seems to exist. The results of the fit function $y = x^m e^b$ are $m = -1.036 \pm 0.081$ and $b = 13.85 \pm 0.32$, which is a fairly good fit. Unfortunately, fiber pieces that are much shorter than 14 cm are not possible to test with this setup because of the size of the temporary fiber holders and the resulting handling in case of such a short fiber. If this power function relation holds true for much shorter fiber pieces the time until a fiber degraded to 5% of its initial transmission could be increased by a lot.

5.4.3 mode conversion

I found that the polymer coating of the tested fibers helps to remove cladding modes from the fiber. A 1m Ge-doped fiber that had its coating completely removed shows a beam profile with a gaussian beam shape superimposed by a speckle pattern known from multimode fibers. More interestingly, such a prepared fiber does not seem to show any of the transmission degradation behavior (measured in the nearfield) observed for the unprepared fibers. The measured transmission even increased slightly with

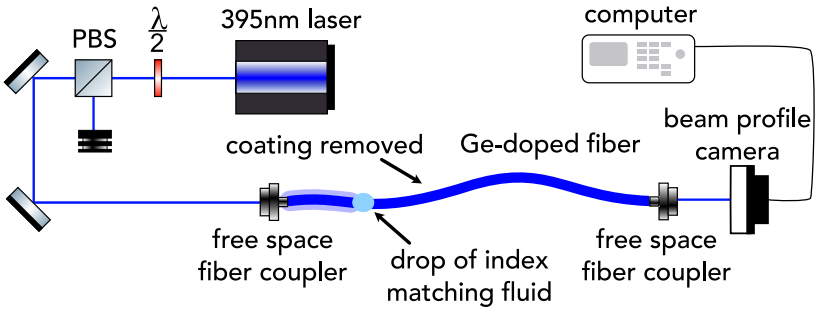

Figure 5.25: Basic fiber testing setup for testing modified Ge-doped fibers at high 395nm transmission levels. A beam profile camera captures the output beam shape. The fiber coating is almost completely stripped off and a drop of index matching fluid is applied on it.

time. This raised the question if there is some mode conversion occurring such that the core mode is lost in the fiber, but the light still propagates on in the cladding, which would lead to this observation. To evaluate this, the existing setup is modified by replacing the photodiode at the end of the fiber with a beam profiler camera to capture the beam profile over time, as illustrated in Figure 5.25.

An 1.5 m fiber test piece is modified by stripping most of its polymer coating, leaving only 15 cm on the incoupling side covered. A drop of index-matching fluid is applied where the polymer is stripped. The index-matching fluid has a refractive index close to that of the silica, so the cladding is arbitrarily expanded at this point and the cladding modes are filtered out. This is also visible with the naked eye, as the drop lights up bright when light is coupled into the fiber. The idea is by completely removing the cladding modes in the first 15 cm of the fiber and leaving the rest of the fiber without the polymer coating, that if there is some mode conversion happening, one should see it in an evolving beam shape. The power after the fiber is adjusted to 30 mW and a correct beam profile camera exposure is set by using neutral density filters. Although the transmission reduced significantly over the course of 1.5 hours, the beam profile did not change. The Gaussian beam shape remained the same for the complete measurement, and no speckle pattern evolved which would be expected for a mode conversion.

5.5 Discussion

This section attempts to explain the observations and findings of the previous sections on the basis of existing literature, conversations, and experiences of other groups.
The principal observation is that all Ge-doped nanofibers subjected to our testing exhibited a discernible pattern of transmission degradation for 399 nm light coupled into the fiber at a maximum power of 440 µW. While the first nanofiber with a waist of $d = 100$ nm tested in chapter 5.3.1 under normal ambient conditions showed a very stable transmission first and a spontaneous start of transmission degradation with a very fast exponential decay, the other two nanofibers with a waist of $d = 200$ nm tested in vacuum showed a less clear and much slower degradation behavior. Numerous transmission tests with only the bare Ge-doped fibers complement these observations that there are some underlying degradation processes of the fiber material itself which changes the light propagation of the fiber for 399 nm and 395 nm light.

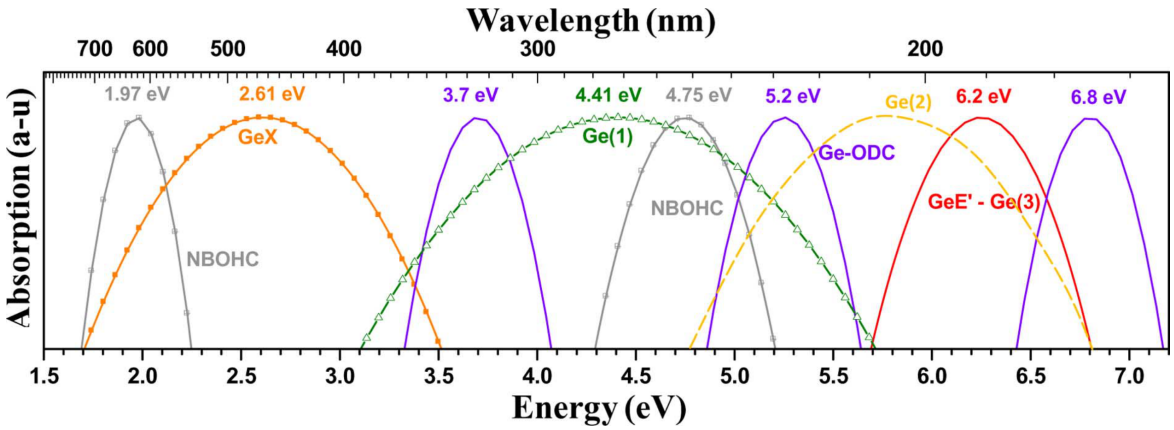

Figure 5.26: Germanosilicate absorption centers, taken from [45]

For more than 50 years it has been shown that electromagnetic radiation degrades the optical properties of fibers in very complex ways. One of them is called radiation-induced attenuation (RIA) [45, 46]. It corresponds to the observations made in the previous sections, a decrease in transmission capability of the fiber induced by radiation, in our case near UV light. The response of a fiber to radiation is still too complex to be fully predictable, which is why testing of fibers for a specific use case under certain conditions is often still a necessity. Starting in the near-UV range, Ge-doped fibers show a photoinduced color-center formation, often also called solarization. The photon energy is high enough to create color centers, which are localized defects in the silica structure that can absorb photons and lead to an attenuation of the transmission [47]. This occurs because of interaction with the dopant, other impurities present in the silica glass, or the strained molecular bonds that can develop during the fiber drawing process [48, 49]. L. J. Poyntz-Wright et al. [50–53] found that for short Ge core doped fibers a few meters long and irradiated at modest power levels of the order of 100 $\mathrm{mW}/\mu\mathrm{m}^2$ in the 420 to 540 nm spectrum lead to a spontaneous increase in loss over time of irradiation in this spectrum. They explain this non-linear behavior by two-photon absorption (TPA), which enables photons in the blue/green to reach UV energy levels that lead to the formation of color centers in the silica matrix. These color centers lead to an increase in absorption in the tested spectrum. Even though their tests were limited to this range because of their laser setup, this might also apply to the wavelengths I tested for the fibers, because as figure 5.26 shows, the absorption centers of such defect structures have quite a large linewidth.

Photoinduced refractive index changes can also be a source for the observations made, as Ge-doped fibers are known for their photosensitivity[54]. This photosensitivity can be exploited to create narrowband fiber Bragg reflectors [55, 56]. Such a Bragg reflector inside a fiber can be created by a weak standing wave intensity pattern of 488 nm light propagating along the fiber axis. The standing wave pattern evolves by interference between the forward propagating beam and Fresnel reflection on the fiber endface. The Bragg reflection evolves in a matter of minutes in the experiment presented by K. O. Hill et al. [54] and led to a back reflection of the exposure wavelength with nearly 90% efficiency. The localized heating of a Ge-doped fiber with a hydrogen rich flame, which resembles the nanofiber fabrication process, also leads to an increase in photosensitivity for Ge-doped fibers by a

factor greater than ten in the UV as F. Bilodeau et al. [57] found out.

This is consistent with what a fiber manufacturer wrote us upon our request for Ge-doped fibers suitable for 399 nm and 395 nm. Exail (former iXblue) wrote us that they observed strong solarization for Ge-core doped fibers after a few tens of milliwatts of injected light at around 400 nm in multiple projects, which led to an attenuation of the signal of several dB/m. That is why they do not sell or fabricate any Ge-doped fiber for the near-UV range. Other fiber manufacturers such as OZ optics [58] and Fibercore [59] also only offer pure silica fibers for use at and below 400 nm. This statement from Exail and the offerings from other companies support the unfavorable usability of Ge-doped fibers at 399 nm and 395 nm light for an extended time period, even at low power levels of a few tens of milliwatts.

On another occasion at the ”Optical Nanofibre Applications: From Quantum to Biotechnologies (ONNA 2025)” meeting in March 2025 we had a poster with my findings regarding the transmission degradation of Ge-doped fibers at 399 nm and 395 nm. There we met Stéphane Trebaol from the Institut Foton in Rennes, France, who told us that they observe similar transmission degradation with Ge-doped fibers in the near UV region. They tried to find a solution or explanation for these processes too, but did not manage to do so up to that point.

CHAPTER 6

Ideas for alternative solutions

As chapter 5 showed, germanium core doped fibers are not the best candidates for transmitting 395 nm and 399 nm light for extended time periods, due to the observed degradation behavior. Therefore, alternative solutions need to be developed.

Currently, we have three different new concepts in various stages of development that I actively developed or helped to develop and evaluate. In the following, the current development status of these ideas is discussed and how likely they might become a solution for the project. All of these concepts are based on the general knowledge in the community that pure silica fibers consisting of an undoped pure silica core and a fluorine-doped cladding or in the case of photonic crystal fibers pure silica cladding, are better suited for UV applications as they are less prone to degradation due to UV light [46, 60–62]. These step index fibers, often also called flourine-doped (meaning doped cladding) or pure silica (meaning silica core) fibers in the literature, still show degradation processes in the deep UV spectrum, but on a much longer timescale and higher power levels than Ge-doped fibers [14, 46, 60].

6.1 F-doped nanofiber fabrication

The most obvious solution would be to fabricate a nanofiber from F-doped fibers, as they provide increased resistance to UV light. However, this is something the Berlin group has already attempted multiple times without success. Early in the nanofiber pulling process, the transmission of the fiber across the complete spectrum drops, even before reaching tens of micrometers in diameter. This is unexpected, as the fabrication principle should be exactly the same as that for the Ge-doped fibers. Currently, there are two proposed explanations for this behaviour. The first being that the hydrogen flame they use for the pulling process is reacting with the fluorine in the cladding in a way that the fluorine evaporates, such that the refractive index changes in the heated area and disturbing the total internal reflection at the cladding interface. The consequence would be that the mode expands uncontrolled and is lost.

The second possible explanation is that the fluorine dopant is present only in the immediate vicinity of the core of the tested fibers but is not distributed uniformly from the inside to the outside of the cladding. It might also be that around the F-doped silica cladding there is again pure silica. If the fiber is used for its designed purpose in its designed wavelength range, this will never cause a problem because the mode field does not expand very far into the cladding. However, in the fiber-tapering process, the light mode will eventually expand beyond this doped region in the cladding. This will again act as a refractive index change which disturbs the desired mode expansion as it transitions from the core/cladding confinement to an air/cladding confinement. The consequence is that the mode expands uncontrollably and is lost.

Both explanations are based on observations and experiences from the group in Berlin. I contacted multiple fiber manufacturers to obtain a statement on the silica composition of their F-doped fibers, but they did not comment on that or respond to the request. There are no cases of succesfully fabricated F-doped nanofibers in the literature.

In literature [63–67] the fabrication of F-doped optical fibers and their preforms is described. A fluorine-doped cladding is often surrounded by another layer of pure silica, sometimes called overcladding or secondary cladding, which has multiple purposes. It can act as mechanical and environmental protection and, depending on the manufacturing process, is even needed to prevent dopant diffusion or contamination during high-temperature processing of the preform. Also, for the modified chemical vapor deposition (MCVD) process, where different layers of material are deposited inside a silica tube, this manufacturing process leads just by definition to an outer silica layer.
Therefore, the second possible explanation might actually provide the answer why the F-doped nanofiber fabrication is not working as expected, since the tested fibers (Thorlabs SM400) supposedly do not have a fully doped cladding. Finding a fiber where the cladding is fully fluorine doped silica could be the solution, but because the manufacturers tend to not communicate the manufacturing details on those fibers, the research has not been successful yet.

Even if a full fluorine doped cladding fiber fiber can be found, the possibility of an evaporating dopant could still be concerning. If it turns out that there is still a problem with the flame brushing technique and certain silica types, we have already investigated and researched other fabrication techniques that might be suitable to try. Alternative solutions are, for example, indirect heating of the fiber with a slotted sapphire tube around the fiber that is heated with a CO2 laser [68]. This provides a more uniform local heating source with less or close to zero airflow interference and no fiber pollution due to combustion residues compared to the flame brushing technique.
Another indirect heating technique uses an electric ceramic microheater [69]. The heating element is slotted to insert the fiber from the side. They achieve a very uniform temperature distribution in the heating region which can be controlled very precisely, reaching up to 1160 degrees Celsius. Nanofibers manufactured with this technique exhibit a very high transmission of up to 99% [69].

Due to the current lack of a suitable fiber and the expenditure of building a new fiber pulling setup with a microheater or a sapphire tube and a CO2 laser this idea is still in an early development stage. Therefore, future work will initially focus on two other ideas that are easier to implement and test, at least initially, because there are currently no new findings regarding F-doped fiber pulling.

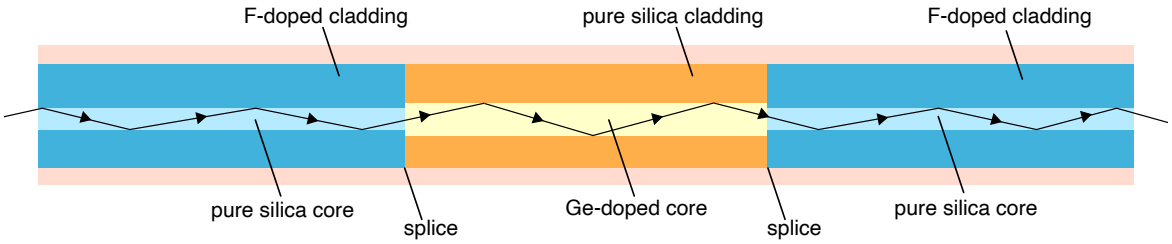

Figure 6.1: Illustration of a Ge-doped fiber piece spliced in between two F-doped fiber pieces. Their repective used material for core and cladding are labeled.

6.2 Splicing F-doped to Ge-doped fiber

An idea that could directly be worked on came from one of the collaborating partners, Arno Rauschenbeutel, of the Berlin group. The data from Section 5.4.2 suggests a fiber length dependence on how fast transmission degradation evolves. However, this leads to the idea of reducing the Ge-doped fiber length as much as possible so that it is still usable to fabricate a nanofiber from it. This small fiber piece is then spliced in between two longer F-doped fiber pieces, which should show a much weaker UV degradation process. So, it essentially combines the features of Ge- and F-doped fibers to create a fiber from which a nanofiber can be fabricated that does not degrade on such small timescales as that seen in Section 5.3. A sketch of this concept is shown in Figure 6.1.

According to Thomas Hoinkes from the Berlin group[1], 3 cm of Ge-doped fiber as an intermediate piece is enough to pull a nanofiber from. To find a suitable F-doped fiber that matches the core diameter of 2.1um and the NA of 0.130 of the Coherent 405HP Ge-doped fiber, an extensive market research was conducted. This leads to three suitable candidates which were chosen by their explicitly given core diameter and NA, or if this is not given by the wavelength range, they are designed for and the given MFD. All of the fibers are single mode and not polarization maintaining. The fibers are a Thorlabs SM300, an OZ optics QSMF-400/650-3/125-0.25-L and an OZ optics QSMF-320-2/125-0.25-L. The Thorlabs fiber was initially chosen because of its easy availability through Thorlabs and similar wavelength range and cutoff wavelength. The core diameter is not given. The OZ optics fibers were ordered later on to extend the testing with fibers that have a core diameter given in their spec sheet that might help to better match the MFD of the Ge-doped fiber.

6.2.1 Splicing loss

In this context, splicing means fusing two optical fiber ends permanently with the goal of creating a single optical fiber. This is done by melting the fiber ends with a very localized heat source and fusing them together. In most of the so-called fusion splicers, an electric arc provides the heat. This process

[1] This was part of a discussion I had in a meeting with him

needs to be done very precisely, to achieve a high overlap of the mode fields of the fiber. Any axial shift or tilt of the fiber ends leads to losses, which is why modern precision fusion splicers have an active control system to align the cores of both fiber ends to each other and adjust the power of the electric arc while fusing.

Figure 6.1 also illustrates that one of the problems with this approach of three pieces of fiber is that the diameter of the core between different fibers can vary a lot. Together with the numerical aperture of the fiber, it defines the mode field diameter. A mismatch between the mode field diameters leads to losses at the splicing point that reduce the overall transmission of the fiber. A low loss is especially important for the 399 nm probe light as it is used for the Rydberg state detection. Every loss after the Rydberg interaction reduces the photon detection efficiency.

As it is of great interest for the experiment to reduce any losses occuring along the fiber, fusion splicing experiments are conducted to evaluate transmission losses between the Ge core-doped fiber (Coherent 405HP) and a cladding-doped fiber (Thorlabs SM300). A total of six splices are performed for each measurement. All splices are performed using the automatic mode of a Fujikura 90S+ fusion splicer, which autonomously adjusts the fusion parameters during the splicing process and features automatic core alignment [43].

In the first set of measurements, 399 nm light is coupled into a 50 cm cladding-doped fiber and spliced to a 50 cm Ge core-doped fiber. Before splicing, the transmission is maximized, with a power input in front of the fiber of $(585.1 \pm 0.2)\,\mu W$ and a measured power output of $(116.2 \pm 0.4)\,\mu W$. After splicing, the output power is measured, and the fiber is cut, cleaved, and spliced again. The mean output power after all six splices in this configuration is $(86.8 \pm 0.2)\,\mu W$, corresponding to an approximate transmission loss of 25.3%.

In the second set of measurements, the procedure is repeated in the reverse direction. Light is coupled into the Ge core-doped fiber, which is then spliced to a cladding-doped fiber. An input power of $(550.4 \pm 0.2)\,\mu W$ and an output power of $(105.3 \pm 0.4)\,\mu W$ are measured prior to splicing. The mean output power after all six splices in this configuration is $(83.8 \pm 0.2)\,\mu W$, corresponding to an approximate transmission loss of 20.4%.

According to the theory [17], the order of the fibers should not make a difference for the light propagation, as the mode overlap is the same in both directions. However, the core and cladding doping between the fibers differs, and therefore also the refractive indices, which might result in this directional splice loss difference of about 4.9%.

A full test fiber with a three-centimeter Ge-doped fiber piece spliced between two F-doped fiber pieces (SM300) has a calculated transmission loss of (40.5 ± 0.2) %. The mean transmission loss from three separate measurements is (40.1 ± 0.4) % which shows experimental agreement. Figure 6.2 shows such a combined fiber, in which the loss of the splices can be seen. The last SM300 fiber piece lights up the brightest, probably due to cladding modes that still propagate in the Ge-doped piece, but get lost after the splice to the SM300 piece.

To differentiate intrinsic splicing loss due to different fiber characteristics and extrinsic factors such as alignment limitations of the splicer itself, the fiber-to-fiber splice loss with the same fiber material is measured. In this set of measurements, 399 nm light is coupled into a 50 cm cladding-doped fiber (SM300) and spliced to another 50 centimeter cladding-doped fiber (SM300). The mean transmission

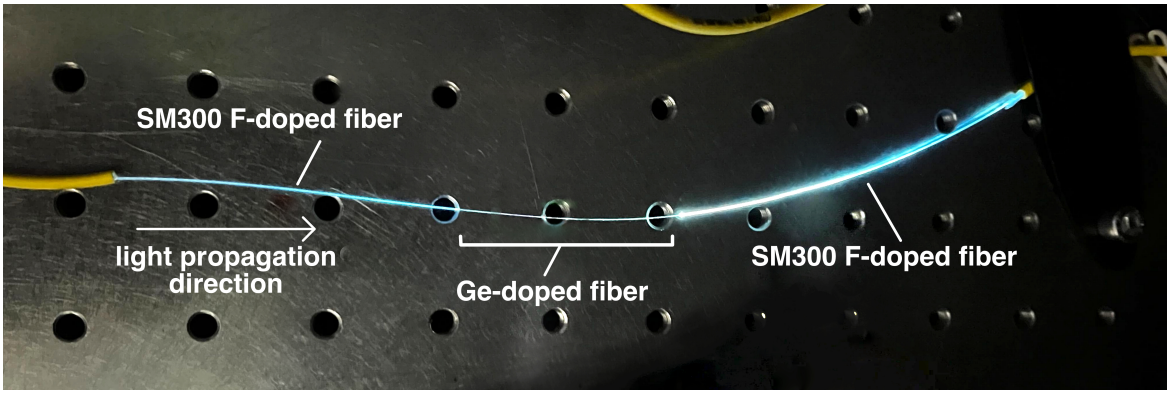

Figure 6.2: A 3 cm Coherent 405-HP Ge-doped fiber piece spliced in between a Thorlabs SM300 F-doped fiber. The position of the splices can be made out by the Thorlabs SM300 fiber pieces glowing.

loss compared to the nominal output of (107.3 ± 0.4) µW after all six splices in this configuration is (9.3 ± 0.2) %. This puts the previously measured values for the splicing losses of different fiber materials in context. It means that this is not exclusively an intrinsic problem of an MFD mismatch and material composition between the different fibers, but also an extrinsic factor of core alignment. This in turn creates two areas that can be further optimized. Having discussed this with the Berlin group, we found that the other splicer in our group, the Fujikura FSM-100P+ [70] is much better suited for such small core diameters of 2.1-3.0 µm. According to them, it provides a higher core alignment accuracy than the Fujikura 90S+ [43] and therefore a lower extrinsic loss. Additionally, it features a tapering function that allows fibers with different mode field diameters to undergo tapering during the splicing process, thereby enabling mode compression and achieving a closer alignment of the MFDs of both fibers. Unfortunately, the Fujikura FSM-100P+ was not available for testing until the end of the research phase.

6.2.2 Transmission test

The combined fiber made from two F-doped fiber pieces (SM300) with a 3 cm Ge-doped fiber spliced in between is tested for its transmission durability. Light is coupled into the fiber from the basic 395 nm laser coupling setup already used for the Ge-doped material tests in Section 5.4. The power in transmission is adjusted to (50.0 ± 0.1) mW to match the power levels in transmission from the Ge-doped material tests. During the following 124-hour exposure time span, the transmission gradually drops to 58% of the initial transmission. Reoptimization of the coupling does not change this outcome. After measurement, it turns out that the transmission power level was actually (90.2 ± 0.1) mW at the start of the measurement, because the powerhead used shows a power level about 55% lower than the actual level. This alters the comparability with the results in Section 5.4, but ultimately does not change the observation of a substantial decrease in transmission. By replacing the Ge-doped fiber piece in between by cutting it off from both F-doped fibers and splicing in a new piece, the transmission loss resulting from the Ge-doped fiber piece is evaluated by comparing it to the transmission with the new piece. Replacing the Ge-doped fiber piece three times leads to a mean transmission loss due to the old 3 cm Ge-doped fiber piece of (0.7 ± 0.1) % after 124 hours of exposure. This means that most of the power loss occurs in the F-doped fiber and only a small to negligible amount is lost in the 3 cm

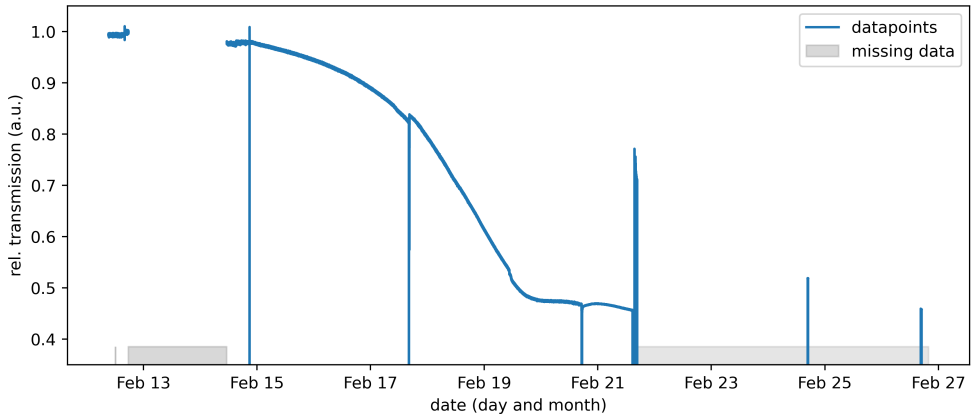

Figure 6.3: 1 m Thorlabs SM300 transmission test at 60 mW of 395 nm in transmission. The relative transmission is plotted against the time as date of the month.

Ge-doped fiber piece, as the observations from Section 5.4 suggest. However, this also means that the SM300 F-doped fiber is also subject to some sort of photodarkening due to the UV light, but on a much larger timescale than the Ge-doped fibers. Chlorine impurities in the silica matrix that lead to absorption at around 400 nm can be a additional cause for this observation [71].

To exclude surface damage on the fiber facet due to high power levels as a main contributor to these degradation observations for the SM300 fiber, another measurement is conducted with a bare 1 m F-doped SM300 fiber. This could not be done before with the three piece spliced fiber. The ends were patch cables with permanent connectors where cutting of the ends is not really a suitable option. The bare 1 m F-doped SM300 fiber is coupled to the 395 nm laser coupling setup, and the power after the fiber is adjusted to (60.0 ± 0.1) mW by increasing the input power. The transmission over time is recorded and shown in figure 6.3. After about 180 hours of continuous exposure, the transmission is reduced to approximately 46.8% compared to the initial transmission. Reoptimization of the coupling does not significantly increase the transmission, as can be seen by the dips to zero and the following transmission level. The overall transmission reduction behavior is similar to that of the fiber spliced together from three separate pieces. Subsequently, the fiber is cut by 4 cm on both sides, recleaved, and recoupled to the optimum. This leads to a jump in transmission between February 21 and February 22. A transmission of approximately 74.2% could be regained after this procedure, leading to the conclusion that a little over half of the power is lost in those 4 cm pieces that were cut off. If this is solely the result of a fiber facet damage due to the high intensity or a degradation inside these 4 cm pieces, has not been investigated at this point. However, the main conclusion from this measurement is that the transmission of the remaining SM300 fiber at a wavelength of 395 nm and a power of 60 mW did degrade over time by at least 25.8% due to some process inside the fiber material. The light exposure continues for five more days and the two spikes from the zero line after February 23 mark measurements of the output power, which continues to decrease while the input power is constant over the whole measurement period.

A future test at lower power levels that match the anticipated power level needed for the main experiment and the evaluation of the lowest possible splicing loss with the high performance Fujikura FSM-100P+

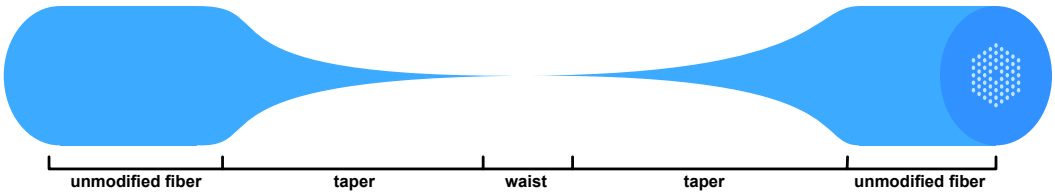

Figure 6.4: Illustration of a tapered photonic crystal fiber showing its facet structure and the typical waist and taper regions of such a fiber.

splicer [70] make this idea still an interesting prospect.

6.3 Photonic crystal nanofiber fabrication

Another idea I had was to try photonic crystal fibers (PCF) [72, 73] as a source material to fabricate nanofibers. Figure 6.4 shows a conceptualized sketch of this idea. Photonic crystal fibers allow single mode transmission across a very broad spectral range, ranging from UV to IR with flexible mode field diameters. They are typically made from pure silica and do not contain any dopant that could cause problems when exposed to UV light or heated by a hydrogen flame. They handle high power levels of 399 nm light without showing any degradation over months [61, 62]. They are different in construction from a conventional optical fiber. Instead of achieving a refractive index contrast by a dopant, a solid silica core area is surrounded by a cladding area made of the same material as the core with many small holes in a hexagonal structure in it.

Figure 6.5 shows a sketched cross section of this type of fiber. The air holes in the cladding region effectively lower the refractive index in the cladding compared to the core. The light propagation may thus be thought of once more as a phenomenon of total internal reflection, owing to the refractive-index contrast. Light propagation in hollow-core photonic crystal fibers is possible as a result of photonic band-gap guidance. They are not of concern for this idea in the current state because of their hollow core structure which we think might make it even harder to fabricate a nanofiber with.

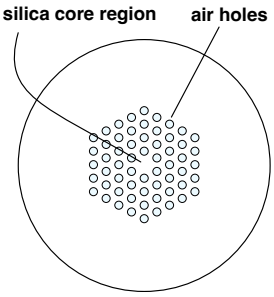

Figure 6.5: Facet structure of a PCF fiber showing the solid silica core area and the hexagonal air hole structure that resemble the cladding.

An extensive literature investigation on the idea led to some groups that have already worked on tapering PCF for different purposes, such as supercontinuous generation [74], but none of them reached an order of magnitude of a few hundred nanometers in waist diameter that can already be manufactured without losses using standard step index fibers [11]. For PCFs, a five-time reduction in waist diameter was achieved compared to the original fiber diameter [75]. The transmission of long wavelengths gets attenuated the lower the waist diameter is tapered, indicating a minimal low-loss waist diameter per wavelength. B. T. Kuhlmey et al. [76] already established this fundamental mode cut-off for photonic crystal fibers where the mode transitions from confinement to non-confinement two years prior. H. C. Nguyen et al. [77] achieved similiar levels in diameter reduction as E. C. Mägi et al. [75].

More interesting is their approach on tapering pure silica photonic wires which have a cladding structure different from that used for PCFs. The silica cladding that surrounds the single layer of air holes is thin compared to the microstructure itself.

Figure 6.6 shows a sketch of the cross sectional structure of the photonic wire used in [77, 78]. They claim that this structure does not exhibit a fundamental mode cut-off like they saw in PCFs even when the structures were tapered to the micrometer scale. The large index contrast structure keeps the mode confined to very small waist diameters. They taper these photonic wires from a diameter of 130 µm to 2.3 µm with still a strong mode confinement and an uncollapsed hole structure. The mode begins to leak out of the structure with further tapering, and 70% of the intensity is outside of the fiber at a ratio of outer diameter (OD) to propagating wavelength λ of 0.6. This result approaches the evanescent field parameters we want for our experiment. By controlled collapse of the hole structure by again heat treating the fiber locally after pulling, they managed to increase the evanescent field outside the fiber even before reaching $\mathrm{OD}/\lambda = 0.6$ [78]. These are promising results for our own endavours. Finding a commercially available photonic wire such as H. C. Nguyen et al. presented was not possible, as such designs are mostly custom-made by other collaborating groups that have the facilities to fabricate optical fibers and their preforms. So we agreed to try to pull photonic crystal fibers with the setup Berlin has.

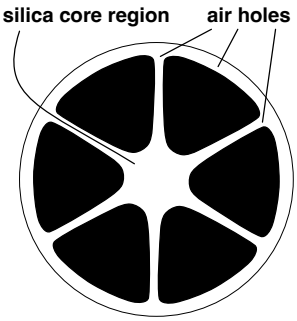

Figure 6.6: Photonic wire cross section depicting the big air holes in the structure that resembles the cladding

NKT Photonics is one of the only manufacturers that sells photonic crystal fibers on a spool in small quantities, so we opted to buy 20 meters of their standard LMA-5 photonic crystal fiber with a hole structure design similar to the one shown in figure 6.5. The idea is to taper the fiber like H. C. Nguyen et al. achieved with the PCF, find the suitable waist diameter before losses below 400 nm begin to rise, and try to combine this with the controlled hole collapse they achieved with the photonic wires [78] to eventually fabricate a photonic crystal nanofiber that reaches the needed evanescent field parameters.

I discussed the progress and possible solutions on how to transfer the work of the other groups [74, 75, 77, 78] onto the tapering process of photonic crystal fibers with Thomas Hoinkes, who fabricates the nanofibers in the Berlin group. Up to the time of writing this thesis, he is able to reproduce the tapering of the PCF to tens of micrometers and, as expected, also observes the loss evolving for longer wavelengths the lower the taper diameter gets. The hole structure remains uncollapsed throughout the tapering process. The wavelength range of interest below 400 nm is currently unaffected by the tapering. This statement is also not completely tenable, as the transmitted power at this wavelength range is very low because the PCF fiber is spliced in between two fiber pieces that have a single-mode cutoff wavelength of 720 nm. This is done to not waste too much of the PCF while still being in an exploratory phase for the pulling parameters.

It turns out that controlled collapse of the air holes in the unpulled and pulled PCF is not trivial because a high flame temperature seems to be needed for both cases. However, this displaces the fiber and deforms the taper region in an uncontrolled and unwanted manner after the pulling process. Splicing the PCF to another fiber, on the other hand, leads to a complete collapse of the hole structure, as can be seen in figure 6.7. A controlled electric arc could be a suitable alternative for collapsing the

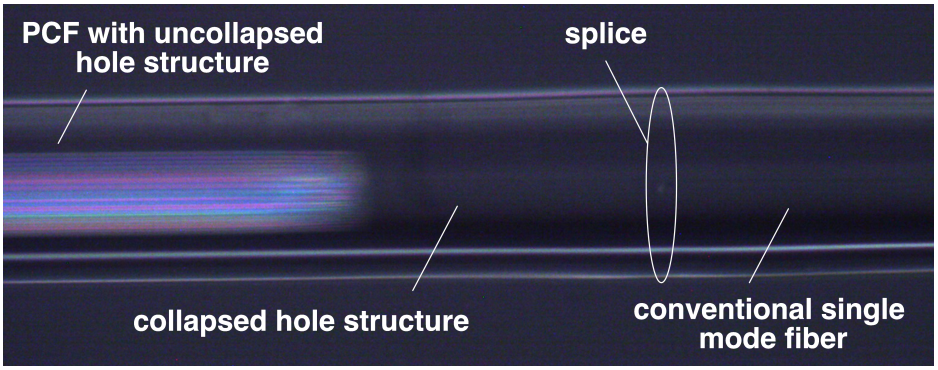

Figure 6.7: PCF fiber spliced to a conventional single mode fiber, showing the collapsed and uncollapsed hole structure. Adapted from: Thomas Hoinkes, Berlin University

holes with a hydrogen flame, as the fiber displacement should be minimal with this method. However, this also requires further testing on a photonic crystal fiber pulled to the micrometer scale. In the next step, they will try pulling a photonic crystal without spliced ends, see how the transmission below 400 nm evolves, and try to collapse the hole structure in a controlled manner. The fiber ends remain open, so that the air in the hole structure equalizes with the ambient pressure while heating to rule out pressure increase inside the air holes while heating the fiber as another problem for the controlled hole collapse.

CHAPTER 7

Conclusion and outlook

As a core part of my thesis, I developed and constructed a fiber testing setup in which nanofibers can be tested. I presented the finished setup in chapter 4. The setup reached a fully functional and easy-to-use state in which the handling is repeatedly proven to be dust-free. A vacuum chamber with a two-stage evacuation system was built that yielded a successful integration of nanofibers into vacuum down to a minimal pressure of 8.64×10^{-8} hPa. For dust-free fiber handling, I built an inner clean air box that allows easy access to the vacuum chamber to install nanofibers into it. To analyze the transmission of the nanofibers we received from our collaborators, I also built an intensity-stabilized transmission analyzation setup. It proved to be a reliable system with which the transmission of three nanofibers at 399 nm light could be analyzed over several weeks as I showed in chapter 5.
In this second part of my thesis I evaluated the transmission of three nanofibers, one under ambient pressure and two under vacuum conditions. The first fiber showed a spontaneous exponential decay in its transmission after being exposed to 440 µW of 399 nm light for about 1.5 hours. This decay followed a clear exponential trend and resulted in a nanofiber that transmitted less then 30% of its initial power after less than four hours of light exposure to 440 µW of 399 nm light. The second and third nanofiber which were tested in vacuum also showed a loss of transmission over time, but on a timescale of days instead of hours. The shape of this transmission degradation curve for both nanofibers did not resemble that of the first tested nanofiber. An initial phase of a fast decay within a few hours was followed by a slower decay over a multitude of days and weeks settling at relative transmission levels of 24.2% for the second and 47.6% for the third nanofiber. Going further, I found out that this degradation behavior also shows up for unmodified Ge-doped fibers at 399 nm and 395 nm light. Numerous tests to find systematic correlations were conducted showing that these fibers also exhibit many obscure behaviors.

In the last weeks of my thesis I investigated ideas on how to circumvent the problem of the degrading fibers for the experiment and worked on three possible solutions in chapter 6. The most promising solution might be the nanofiber fabrication from photonic crystal fibers as the provide a pure silica core and no dopant in the cladding making it more UV resistant than the Ge-doped fibers tested before. After completion of my thesis, the idea of fabricating photonic crystal nanofibers is still far from being at a level comparable to that of conventional nanofibers, but it is a promising basis on which to continue working to find a fabrication route that works for this type of fiber.

Bibliography

[1] A. G. J. MacFarlane, J. P. Dowling and G. J. Milburn,
Quantum technology: the second quantum revolution,
Philosophical Transactions of the Royal Society of London. Series A: Mathematical, Physical and Engineering Sciences **361** (2003) 1655, Publisher: Royal Society, (visited on 01/06/2025).

[2] D. E. Chang, V. Vuletić and M. D. Lukin, *Quantum nonlinear optics — photon by photon*,
Nature Photonics **8** (2014) 685, Publisher: Nature Publishing Group, (visited on 03/06/2025).

[3] F. Flamini, N. Spagnolo and F. Sciarrino, *Photonic quantum information processing: a review*,
Reports on Progress in Physics **82** (2018) 016001, Publisher: IOP Publishing,
(visited on 03/06/2025).

[4] J. M. Raimond, M. Brune and S. Haroche,
Manipulating quantum entanglement with atoms and photons in a cavity,
Reviews of Modern Physics **73** (2001) 565, Publisher: American Physical Society,
(visited on 03/06/2025).

[5] O. Firstenberg, C. S. Adams and S. Hofferberth,
Nonlinear quantum optics mediated by Rydberg interactions, Journal of Physics B: Atomic, Molecular and Optical Physics **49** (2016) 152003, Publisher: IOP Publishing,
(visited on 03/06/2025).

[6] J. D. Pritchard, K. J. Weatherill and C. S. Adams, "Nonlinear optics using cold rydberg atoms",
Annual Review of Cold Atoms and Molecules, vol. Volume 1,
Annual Review of Cold Atoms and Molecules Volume 1, WORLD SCIENTIFIC, 2012 301,
ISBN: 978-981-4440-39-4, (visited on 03/06/2025).

[7] J. Kumlin et al., *Quantum optics with Rydberg superatoms*,
Journal of Physics Communications **7** (2023) 052001, Publisher: IOP Publishing,
(visited on 31/05/2025).

[8] M. Saffman, *Quantum computing with neutral atoms*, National Science Review **6** (2019) 24,
(visited on 04/06/2025).

[9] N. Stiesdal et al., *Observation of collective decay dynamics of a single Rydberg superatom*,
Physical Review Research **2** (2020) 043339, Publisher: American Physical Society,
(visited on 03/06/2025).

[10] A. S. Sheremet, M. I. Petrov, I. V. Iorsh, A. V. Poshakinskiy and A. N. Poddubny,
Waveguide quantum electrodynamics: Collective radiance and photon-photon correlations,
Reviews of Modern Physics **95** (2023) 015002, Publisher: American Physical Society,
(visited on 01/06/2025).

[11] R. Finkelstein et al.,
Super-extended nanofiber-guided field for coherent interaction with hot atoms,
Optica **8** (2021) 208, Publisher: Optica Publishing Group, (visited on 14/05/2025).

[12] J. Ballato and P. Dragic, *Rethinking Optical Fiber: New Demands, Old Glasses*,
Journal of the American Ceramic Society **96** (2013) 2675, _eprint:
https://onlinelibrary.wiley.com/doi/pdf/10.1111/jace.12516, (visited on 04/06/2025).

[13] E. Hecht, *Optik*, De Gruyter, 2018, ISBN: 978-3-11-052665-3, (visited on 24/05/2025).

[14] E. Shafir et al.,
Performance of an F-Doped Fiber Under Very High Ionizing Radiation Exposures,
IEEE Transactions on Nuclear Science **69** (2022) 2290, (visited on 04/06/2025).

[15] A. W. Snyder and J. D. Love, *Optical Waveguide Theory*, Boston, MA: Springer US, 1984,
ISBN: 978-0-412-24250-2 978-1-4613-2813-1, (visited on 25/05/2025).

[16] B. E. A. Saleh and M. C. Teich, *Fundamentals of Photonics*, 1st ed., Wiley, 1991,
ISBN: 978-0-471-83965-1 978-0-471-21374-1, (visited on 25/05/2025).

[17] A. K. Ghatak and K. Thyagarajan, *An Introduction to Fiber Optics*,
Google-Books-ID: pG34VZMil7IC, Cambridge University Press, 1998, 588 pp.,
ISBN: 978-0-521-57785-4.

[18] H. Lundgaard Sørensen,
Controlling the shape of subwavelength-diameter tapered optical fibers,
PhD thesis: Niels Bohr Institute, Copenhagen University, 2013.

[19] G. Sagué Cassany, *Cold atom physics using ultra-thin optical fibres*,
PhD thesis: Rheinische Friedrich-Wilhelms-Universität Bonn, 2008.

[20] D. Gloge, *Weakly Guiding Fibers*,
Applied Optics **10** (1971) 2252, Publisher: Optica Publishing Group, (visited on 25/05/2025).

[21] F. Warken, *Ultradünne Glasfasern als Werkzeug zur Kopplung von Licht und Materie*,
PhD thesis: Rheinische Friedrich-Wilhelms-Universität Bonn, 2007.

[22] F. L. Kien, J. Q. Liang, K. Hakuta and V. I. Balykin, *Field intensity distributions and polarization orientations in a vacuum-clad subwavelength-diameter optical fiber*,
Optics Communications **242** (2004) 445, (visited on 14/05/2025).

[23] T. Birks and Y. Li, *The shape of fiber tapers*, Journal of Lightwave Technology **10** (1992) 432,
(visited on 25/05/2025).

[24] J. Eggers and T. F. Dupont,
Drop formation in a one-dimensional approximation of the Navier–Stokes equation,
Journal of Fluid Mechanics **262** (1994) 205, (visited on 25/05/2025).

[25] C. Baker and M. Rochette,
A generalized heat-brush approach for precise control of the waist profile in fiber tapers,
Optical Materials Express **1** (2011) 1065, Publisher: Optica Publishing Group,
(visited on 25/05/2025).

[26] J. Love et al., *Tapered single-mode fibres and devices. Part 1: Adiabaticity criteria*,
IEE Proceedings J (Optoelectronics) **138** (1991) 343, Publisher: The Institution of Engineering and Technology, (visited on 25/05/2025).

[27] C. S. Adams, J. D. Pritchard and J. P. Shaffer, *Rydberg atom quantum technologies*, Journal of Physics B: Atomic, Molecular and Optical Physics **53** (2019) 012002, Publisher: IOP Publishing, (visited on 31/05/2025).

[28] T. Gallagher, "Rydberg Atoms", *Springer Handbook of Atomic, Molecular, and Optical Physics*, ISSN: 2522-8706, Springer, New York, NY, 2006 235, ISBN: 978-0-387-26308-3, (visited on 31/05/2025).

[29] M. D. Lukin et al., *Dipole Blockade and Quantum Information Processing in Mesoscopic Atomic Ensembles*, Physical Review Letters **87** (2001) 037901, Publisher: American Physical Society, (visited on 31/05/2025).

[30] E. Urban et al., *Observation of Rydberg blockade between two atoms*, Nature Physics **5** (2009) 110, Publisher: Nature Publishing Group, (visited on 31/05/2025).

[31] E. Vetsch et al., *Optical Interface Created by Laser-Cooled Atoms Trapped in the Evanescent Field Surrounding an Optical Nanofiber*, Physical Review Letters **104** (2010) 203603, Publisher: American Physical Society, (visited on 01/06/2025).

[32] K. S. Rajasree, T. Ray, K. Karlsson, J. L. Everett and S. N. Chormaic, *Generation of cold Rydberg atoms at submicron distances from an optical nanofiber*, Physical Review Research **2** (2020) 012038, Publisher: American Physical Society, (visited on 01/06/2025).

[33] A. Vylegzhanin et al., *Excitation of ^{87}Rb Rydberg atoms to nS and nD states (n68) via an optical nanofiber*, Optica Quantum **1** (2023) 6, Publisher: Optica Publishing Group, (visited on 01/06/2025).

[34] L. Pache et al., *Realization of a magic-wavelength nanofiber-based two-color dipole trap with sub-$/2$ spacing*, 2024, arXiv: 2407.02278[physics], (visited on 01/06/2025).

[35] G. Sagué, E. Vetsch, W. Alt, D. Meschede and A. Rauschenbeutel, *Cold-Atom Physics Using Ultrathin Optical Fibers: Light-Induced Dipole Forces and Surface Interactions*, Physical Review Letters **99** (2007) 163602, Publisher: American Physical Society, (visited on 01/06/2025).

[36] M. Sumetsky, *How thin can a microfiber be and still guide light?*, Optics Letters **31** (2006) 870, Publisher: Optica Publishing Group, (visited on 14/05/2025).

[37] M. Sumetsky, Y. Dulashko, P. Domachuk and B. J. Eggleton, *Thinnest optical waveguide: experimental test*, Optics Letters **32** (2007) 754, Publisher: Optica Publishing Group, (visited on 14/05/2025).

[38] P. Lunt, *Design and Construction of a new ultracold Ytterbium Experiment for Rydberg Physics*, Master: University of Southern Denmark, 2019.

[39] X. Wang et al., *Two-color ytterbium magneto-optical trap in a compact dual-chamber setup*, Physical Review Applied **23** (2025) 014004, Publisher: American Physical Society, (visited on 31/05/2025).

[40] A. R. Peerzada et al., *Versatile optical fiber feedthroughs for ultra-high vacuum applications*, Vacuum **180** (2020) 109542, (visited on 04/06/2025).

[41] T. Sun, X. Su, Y. Zhang, H. Zhang and Y. Zheng, *Progress and Summary of Photodarkening in Rare Earth Doped Fiber*, Applied Sciences **11** (2021) 10386, Number: 21 Publisher: Multidisciplinary Digital Publishing Institute, (visited on 04/06/2025).

[42] J.-R. Lee, D. Dhital and D.-J. Yoon, *Investigation of cladding and coating stripping methods for specialty optical fibers*, Optics and Lasers in Engineering **49** (2011) 324, (visited on 04/06/2025).

[43] *Fujikura Core Alignment Fusion Splicer 90S+ Kit*, Fujikura, URL: https://www.fusionsplicer.fujikura.com/products/fusion-splicer/ (visited on 20/05/2025).

[44] Thorlabs, *Thorlabs - FN96A Guide to Connectorization and Polishing of Optical Fibers*, URL: https://www.thorlabs.de (visited on 15/05/2025).

[45] S. Girard et al., *Radiation Effects on Silica-Based Optical Fibers: Recent Advances and Future Challenges*, IEEE Transactions on Nuclear Science **60** (2013) 2015, (visited on 22/05/2025).

[46] S. Girard et al., *Overview of radiation induced point defects in silica-based optical fibers*, Reviews in Physics **4** (2019) 100032, (visited on 14/05/2025).

[47] L. Skuja, H. Hosono and M. Hirano, "Laser-induced color centers in silica", *Laser-Induced Damage in Optical Materials: 2000*, Laser-Induced Damage in Optical Materials: 2000, vol. 4347, SPIE, 2001 155, (visited on 14/05/2025).

[48] H. Hanafusa, Y. Hibino and F. Yamamoto, *Formation mechanism of drawing-induced defects in optical fibers*, Journal of Non-Crystalline Solids **95-96** (1987) 655, (visited on 22/05/2025).

[49] E. J. Friebele, G. H. Sigel Jr. and D. L. Griscom, *Drawing-induced defect centers in a fused silica core fiber*, Applied Physics Letters **28** (1976) 516, (visited on 22/05/2025).

[50] L. J. Poyntz-Wright, M. E. Fermann and P. S. J. Russell, "Non-linear transmission in germanosilicate fibres at blue/green wavelengths", IEE Colloquium on Non-Linear Optical Waveguides (02/06/88 - 02/06/88), in collab. with L. J. Poyntz-Wright, M. E. Fermann and P. S. J. Russell, 1988, (visited on 14/05/2025).

[51] L. J. Poyntz-Wright, M. E. Fermann and P. S. J. Russell, *Nonlinear transmission and color-center dynamics in germanosilicate fibers at 420–540 nm*, Optics Letters **13** (1988) 1023, Publisher: Optica Publishing Group, (visited on 14/05/2025).

[52] L. J. Poyntz-Wright and P. S. J. Russell, *Spontaneous relaxation processes in irradiated germanosilicate optical fibres*, Electronics Letters **25** (1989) 478, ADS Bibcode: 1989ElL....25..478P, (visited on 14/05/2025).

[53] L. Poyntz-Wright and P. Russell, *Photochromic dynamics and nonlinear transmission at modulated CW blue/green wavelengths in germanosilicate optical fibres*, Electronics Letters **24** (1988) 1054, Publisher: The Institution of Engineering and Technology, (visited on 23/05/2025).

[54] K. O. Hill, Y. Fujii, D. C. Johnson and B. S. Kawasaki, *Photosensitivity in optical fiber waveguides: Application to reflection filter fabrication*, Applied Physics Letters **32** (1978) 647, (visited on 23/05/2025).

[55] B. S. Kawasaki, K. O. Hill, D. C. Johnson and Y. Fujii, *Narrow-band Bragg reflectors in optical fibers*, Optics Letters, Vol. 3, Issue 2, pp. 66-68 (1978), Publisher: Optica Publishing Group, (visited on 23/05/2025).

[56] C. G. Askins, "Periodic UV-induced index modulations in doped-silica optical fibers: formation and properties of the fiber bragg grating", *Defects in SiO2 and Related Dielectrics: Science and Technology*, ed. by G. Pacchioni, L. Skuja and D. L. Griscom, Dordrecht: Springer Netherlands, 2000 391, ISBN: 978-94-010-0944-7.

[57] F. Bilodeau et al., *Photosensitization of optical fiber and silica-on-silicon/silica waveguides*, Optics Letters **18** (1993) 953, Publisher: Optica Publishing Group, (visited on 23/05/2025).

[58] *Fiber Optic Delivery Systems — OZ Optics Ltd.* URL: https://www.ozoptics.com.cn/products/fiber_optic_delivery_systems.html (visited on 21/05/2025).

[59] *Fibercore Single-Mode (SM) Fiber*, URL: https://fibercore.humaneticsgroup.com/products/single-mode-sm-fiber (visited on 21/05/2025).

[60] S. Girard et al., *Recent advances in radiation-hardened fiber-based technologies for space applications*, Journal of Optics **20** (2018) 093001, Publisher: IOP Publishing, (visited on 19/05/2025).

[61] Y. Colombe, D. H. Slichter, A. C. Wilson, D. Leibfried and D. J. Wineland, *Single-mode optical fiber for high-power, low-loss UV transmission*, Optics Express **22** (2014) 19783, Publisher: Optica Publishing Group, (visited on 22/05/2025).

[62] C. P. Gonschior, D. Eimer, K.-F. Klein, T. Sun and K. T. V. Grattan, "Characterization of UV single-mode and low-mode fibers", *Optical Fibers and Sensors for Medical Diagnostics and Treatment Applications X*, Optical Fibers and Sensors for Medical Diagnostics and Treatment Applications X, vol. 7559, SPIE, 2010 171, (visited on 22/05/2025).

[63] P. K. Bachmann, P. E. E. Geittner, D. Leers and H. J. C. Wilson, "Fluorine-doped optical fibre and method of manufacturing such fibre", U.S. pat. 4802733A, U. P. Corp, 1989, (visited on 14/05/2025).

[64] P. K. Bachmann, "Method of manufacturing fluorine-doped optical fibers", U.S. pat. 4468413A, U. P. Corp, 1984, (visited on 14/05/2025).

[65] D. DiGiovanni and R. Windeler, “Manufacture of optical fibers using enhanced doping”, U.S. pat. 20060179888A1, Individual, 2006, (visited on 14/05/2025).

[66] P. Matthijsse, F. Gooijer, I. Flammer, E. Regnier and G. Kuyt, “Fluorine-doped optical fiber”, U.S. pat. 7526177B2, D. C. BV, 2009, (visited on 14/05/2025).

[67] P. Sillard and M. Bigot-Astruc, “Single-mode optical fiber”, U.S. pat. 8798423B2, D. C. BV, 2014, (visited on 14/05/2025).

[68] M. Sumetsky, Y. Dulashko and A. Hale, *Fabrication and study of bent and coiled free silica nanowires: Self-coupling microloop optical interferometer*, Optics Express **12** (2004) 3521, Publisher: Optica Publishing Group, (visited on 15/05/2025).

[69] L. Ding, C. Belacel, S. Ducci, G. Leo and I. Favero, *Ultralow loss single-mode silica tapers manufactured by a microheater*, Applied Optics **49** (2010) 2441, Publisher: Optica Publishing Group, (visited on 14/05/2025).

[70] Fujikura, *Fujikura Specialty Fiber Fusion Splicer FSM-100 series*, Fujikura, URL: https://www.fusionsplicer.fujikura.com/products/specialty-fiber-fusion-splicer-fsm-100-series-2/ (visited on 20/05/2025).

[71] D. L. Griscom, *Trapped-electron centers in pure and doped glassy silica: A review and synthesis*, Journal of Non-Crystalline Solids, SiO2, Advanced Dielectrics and Related Devices **357** (2011) 1945, (visited on 04/06/2025).

[72] J. C. Knight, T. A. Birks, P. S. J. Russell and D. M. Atkin, *All-silica single-mode optical fiber with photonic crystal cladding*, Optics Letters **21** (1996) 1547, Publisher: Optica Publishing Group, (visited on 15/05/2025).

[73] P. Russell, *Photonic Crystal Fibers*, Science **299** (2003) 358, Publisher: American Association for the Advancement of Science, (visited on 15/05/2025).

[74] S. G. Leon-Saval, T. A. Birks, W. J. Wadsworth, P. S. J. Russell and M. W. Mason, *Supercontinuum generation in submicron fibre waveguides*, Optics Express **12** (2004) 2864, Publisher: Optica Publishing Group, (visited on 14/05/2025).

[75] E. C. Mägi, P. Steinvurzel and B. J. Eggleton, *Tapered photonic crystal fibers*, Optics Express **12** (2004) 776, Publisher: Optica Publishing Group, (visited on 14/05/2025).

[76] B. T. Kuhlmey et al., *Microstructured optical fibers: where’s the edge?*, Optics Express **10** (2002) 1285, Publisher: Optica Publishing Group, (visited on 16/05/2025).

[77] H. C. Nguyen et al., *Tapered photonic crystal fibres: properties, characterisation and applications*, Applied Physics B **81** (2005) 377, (visited on 14/05/2025).

[78] E. C. Mägi, H. C. Nguyen and B. J. Eggleton, *Air-hole collapse and mode transitions in microstructured fiber photonic wires*, Optics Express **13** (2005) 453, Publisher: Optica Publishing Group, (visited on 16/05/2025).